

UNIVERSITÀ DEGLI STUDI DI TORINO

Master's Degree in Physics



Master's Degree Thesis

Cosmogenic radioactivity estimate and detection in asteroids and meteorites: application to Bennu (OSIRIS-REx mission)

Supervisor

Prof. Carla TARICCO

Co-supervisor

Prof. Narendra BHANDARI

Candidate

Andrea ANTONIONE

October 2022

Summary

In October 2020, NASA's OSIRIS-REx mission collected surface material from the asteroid Bennu with the aim of returning it to Earth in late 2023. Like every celestial body in the heliosphere, Bennu is constantly hit by a stream of cosmic rays, which, as it interacts with the atoms within the material, produces isotopes of various elements. Some of these nuclei are radioactive and find wide use in numerous areas of research. In particular, radionuclides of different half-lives can be studied to determine the cosmic-ray exposure history of the object to which they belong. In climatology, cosmogenic radioactivity is exploited to indirectly study solar activity variations, which modulate the cosmic ray flux itself.

In this thesis, the depth-dependent radioactivity trend of different nuclides in Bennu is calculated with two methods: the first, based on so-called physical and semi-empirical models, has already been widely used; the second, a Geant4 simulation, is new in this field. The aim is to estimate the radioactivity of the sample and the time of measurement required to reveal its radioactivity. The measurement will be performed using γ -ray spectrometers at the Monte dei Cappuccini Laboratory in Turin, Italy.

The new method for the radioactivity calculation is validated by the application to different meteorites and the reproduction of experimental data.

Acknowledgements

First, I must thank Prof. William V. Boynton (University of Arizona) for proposing to my supervisor's group to collaborate on this exciting research, and my supervisors, Prof. Carla Taricco and Prof. Narendra Bhandari, for their efforts in guiding me through my thesis.

I must extend my thanks to Prof. Massimiliano Manfrin and Prof. Massimo Masera for providing me with the computational resources needed for this project, to Prof. Paolo Colombetti for his guidance in the Monte dei Cappuccini Laboratory, and to Dr. Ilaria Bizarri and Dr. Dario Barghini for their valuable advice.

I have to say a huge thank you to my girlfriend R.M. and my friends for their support and role in my life. We have had thousands of adventures, and many more await us.

Last, I thank my father and my mother, whose support in moments of weakness has been and always will be crucial in my life.

Thanks!
Andrea Antonione

Table of Contents

Abbreviations	VI
Introduction	2
1 NASA’s OSIRIS-REx mission	5
1.1 Asteroid Classification	6
1.1.1 Orbit-based classification	7
1.1.2 Composition-based classification	9
1.2 The asteroid Bennu	9
1.3 Sample acquisition	12
2 Activity measurements at Monte dei Cappuccini Laboratory	16
2.1 GEM 150 gamma-ray spectrometer	17
2.2 Study of the sample container	19
3 Cosmogenic radionuclides in asteroids and meteorites	21
3.1 Solar activity and its variations	22
3.2 Cosmic Rays	23
3.2.1 Solar Cosmic Rays (SCRs)	25
3.2.2 Galactic Cosmic Rays (GCRs)	25
3.2.3 GCR flux parametrizations	26
3.2.4 Modulation parameter	28
3.3 Cosmogenic radioisotopes	33
3.3.1 Production and secular equilibrium	34
3.3.2 $^{22}\text{Na}/^{26}\text{Al}$ activity ratio	36

4 Cosmogenic radionuclides production models	39
4.1 SCR production	41
4.2 GCR production - physical model	42
4.3 Total production	44
4.4 GCR production - Geant4 model	45
4.4.1 The code	46
4.4.2 Particle generation	47
4.4.3 Secular equilibrium-related modulation parameter	50
4.4.4 Physics list selection	52
5 Results and comparisons of the models	59
5.1 Results of the Geant4 simulation	59
5.2 Comparison of the models	63
5.3 Reproducion of $^{22}\text{Na}/^{26}\text{Al}$ trend	65
5.4 Sample radioactivity and ^{26}Al saturation	68
6 Conclusions	72
6.1 The Geant4 model	72
6.2 Activity of the sample	73
7 Future plans	74
A Classification of meteorites	77
List of Tables	81
List of Figures	82
References	86

Abbreviations

BERT	Bertini
BIC	Binary Ion Cascade
CME	Coronal Mass Ejection
CPD	Counts Per Day
CS	Current Sheet
FTF	Fior tof
GCR	Galactic Cosmic Ray
HMF	Heliospheric Magnetic Field
HPGe	Hyperpure Germanium
INAF	National Institute of Astrophysics
INCL	Liège Inter-Nuclear Cascade
ISN	International Sunspot Number
LINEAR	Lincoln Near-Earth Asteroid Research
MOID	Earth Minimum Orbit Intersection Distance
NEA	Near-Earth Asteroid
NEO	Near-Earth Object

OFHC Oxygen-Free High-Conductivity

PHA Potentially Hazardous Asteroid

PHO Potentially Hazardous Object

PMT Photomultiplier

PSFD Particle Size-Frequency Distribution

QGS Quark Gluon String

SCR Solar Cosmic Ray

SEP Solar Energetic Particle

SN Sunspot Number

Introduction

OSIRIS-REx is a NASA asteroid sample-and-return mission meant to collect surface material from the asteroid Bennu. The purposes of the mission are to study the formation and evolution of the solar system and its initial stages of planet formation and to search for organic compounds which could contribute to the explanation of the origin of life on Earth. The Monte dei Cappuccini Laboratory in Turin (Italy), led by Prof. C. Taricco and with whose research group I collaborated for my thesis, devoted more than three decades in meteorites analysis and has been chosen by NASA to carry out radioactivity analysis on the sample, which will provide information about the cosmic-rays exposure history of the asteroid.

The cosmic radiation flux reflects the solar activity variations. In particular, there is an anti-correlation between the intensity and energy spectrum of galactic cosmic rays (GCRs), the component of the radiation that originated outside the heliosphere, and the interplanetary magnetic field intensity. The interaction between cosmic rays and interstellar matter leads to the production of isotopes of different elements, including some radioactive nuclei useful for the determination of the exposure history of the considered celestial body. The concentration of a cosmogenic radionuclide derives from the balance between the production due to cosmic rays and the destruction due to radioactive decay. The measurement of the radioactivity of isotopes with different half-lives allows for reconstructing the cosmic radiation flux intensity at different time scales, which represents the exposure history of the studied body and leads to the determination of the solar activity variations through time.

In the climatology field, studying solar activity variations at different time scales is crucial for a better understanding of the Sun's influence on Earth's climate

and the dynamics inside of the star itself. The radioactivity measurements in the extraterrestrial matter have the purpose of solving the biases problem in the studies of terrestrial archives, whose proxies are influenced by various Earth phenomena, such as geomagnetic field oscillations and deposition rate variations, causing differences between results from different archives, and extending the information about solar activity back in time, beyond the limit of the 17th century related to the sunspot number series.

My thesis consists in the study of radionuclides production in asteroids and meteorites, with a particular focus on Bennu. Part of this work has been presented at the ORISIS-REx Sample Analysis Meeting in Tucson ("Gamma Counting of Cosmic-Ray Produced Nuclides in Bennu", by W. Boynton et al.).

Two approaches in parallel were applied for the radioactivity estimation of the OSIRIS-REx mission sample: the so-called physical and semi-empirical models, already widely used in this field for years, and a Geant4-based simulation, new in this area of research. This new model is validated by comparing the results of the two approaches, the agreement with experimental data, and the reproduction of the $^{22}\text{Na}/^{26}\text{Al}$ radioactivity ratio trend over the past 80-90 years. The model can be used for calculating the radioactivity in a celestial body with a known solar activity intensity or, on the contrary, deducing the latter from the former. In the end, future plans are explained.

In Chapter 1, a general description of the classification of asteroids and in which category Bennu falls is given, with more details about the asteroid target of the mission. A short description of NASA's OSIRIS-REx mission and the sampling operations is provided.

In Chapter 2, the facility and the detectors at Monte dei Cappuccini Laboratory are described, and the study on the sample geometry for the radioactivity analysis is presented.

In Chapter 3, the link between the flux of cosmic particles and solar activity variations is described, with a first insight into the production of radionuclides in celestial bodies.

In Chapter 4, the models of radionuclides production are presented, including

some results about the radioactivity trend in the asteroid. The final results, including the expected radioactivity of the sample, are shown in Chapter 5.

Finally, in Chapters 6 and 7, the conclusions and future plans are exposed.

Chapter 1

NASA's OSIRIS-REx mission

The "Origins Spectral Interpretation Resource Identification Security Regolith Explorer" (OSIRIS-REx) is a NASA asteroids study mission, the third in the New Frontiers program [23]. If successful, it will be the first U.S. mission to return a sample from an asteroid. The spacecraft (Figure 1.1) was launched on September 8, 2016, from Cape Canaveral, and after a two-year journey, it reached Bennu. On December 3, 2018, the probe began orbiting the object and performing spectral analyses on its surface to find a suitable sampling site and study the Yarkovsky effect, such as the force acting on a spinning body due to the anisotropic emission of thermal photons [10]. On October 20, 2020, OSIRIS-REx collected (250 ± 101) g of surface material [22] with its Touch And Go Acquisition Mechanism (TAGSAM) [8], such as a robotic arm that reached the asteroid and sampled the first centimeters of surface [47]. After leaving the asteroid at the beginning of May 2021, the mission is scheduled to return to Earth on September 24, 2023, after which it will immediately begin its new journey to the asteroid Apophis for further studies.

The sampled material is expected to unravel information about the birth and evolution of the Solar System and its initial stages of planet formation. Scientists hope to find sources of organic components that could contribute to the explanation of the beginning of life on Earth.

In this chapter, the classification of asteroids and in which category Bennu falls are described, and some information about the sample collection are given. For a more detailed description of the mission, the spacecraft, and the sample acquisition, refer to Lauretta et al. (2017, 2022) [23][22], and Bierhaus et al. (2019) [8].

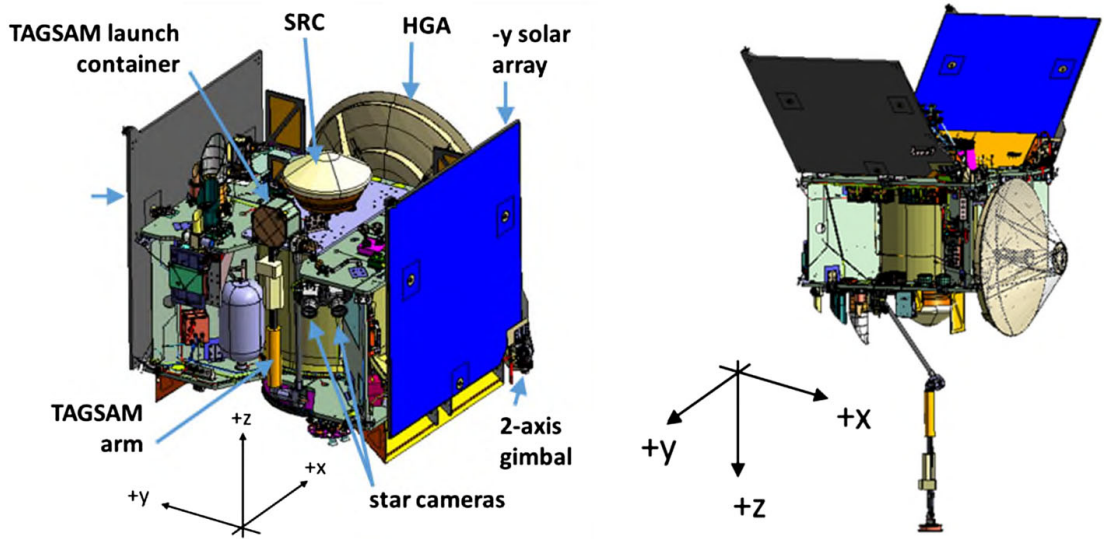


Figure 1.1: The OSIRIS-REx spacecraft in launch configuration (left) and sampling configuration (right). Image adapted from Bierhaus et al. (2018) [8].

1.1 Asteroid Classification

Asteroids are minor planets, lacking atmosphere, consisting of rocky remnants of the early formation of our Solar System, and ranging between a few meters to hundreds of kilometers in diameter. Objects with size less than 1 meter are classified as meteoroids [36]. Asteroids are, with some exceptions (like Ceres, the most massive asteroid with a 476 km equatorial radius), irregularly shaped, characterized by a cratered surface, and rotate on themselves.

Two classifications of these objects can be distinguished by basing on the region of the Solar System in which they orbit or by basing on the chemical composition.

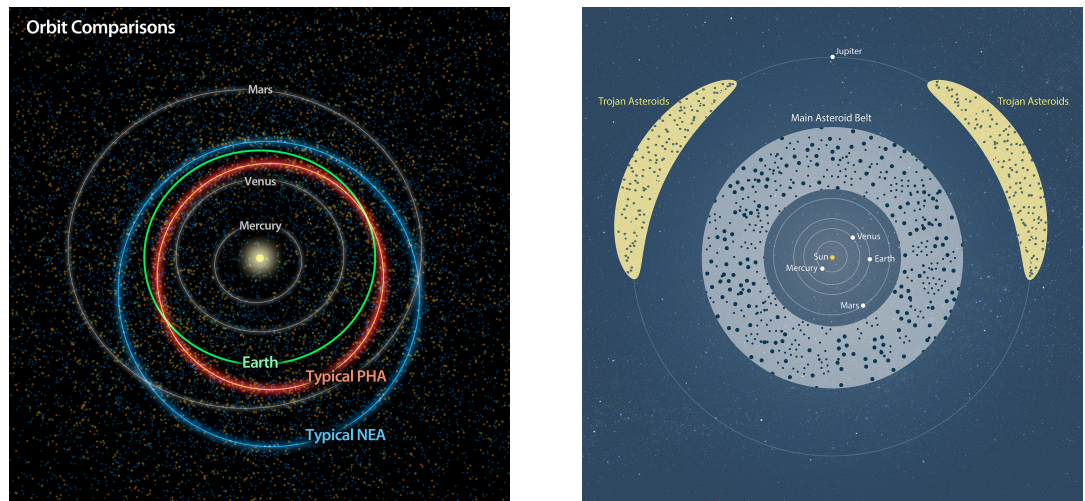
1.1.1 Orbit-based classification

This classification is related to the region in which asteroids orbit the Sun.

- *Near-Earth Objects (NEO)* are bodies orbiting the Sun with a perihelion less than 1.3 AU. Near-Earth Asteroids (NEA) are asteroids that satisfy the previous condition. NEOs with a Minimum Orbit Intersection Distance (MOID) from Earth of 0.05 AU or less and an absolute magnitude of 22 or less are classified as Potentially Hazardous Objects/Asteroids (PHO/PHA), which means that they can make close approaches to the Earth during their revolving, and their size is such (at least 140 m of diameter) that it can create serious damage in the event of an impact. See Table 1.1 for the classes of NEA and Figure 1.2.a for the typical NEA and PHO orbits.
- *Main Belt Asteroids* orbit between Mars (1.524 AU) and Jupiter (5.209 AU) and represent the majority of known asteroids (75%) (Figure 1.2.b). Most of the Main Belt Asteroids are concentrated between 2.12 AU and 3.3 AU. Large objects like Ceres, Vesta, Pallas, and Hygiea are in this region.
- *Trojan Asteroids* share their orbit with a larger planet, such as Jupiter (mostly), Neptune, etc., but do not collide with it because they gather around the so-called L₄ and L₅ Lagrangian points of stability, where the gravitational pull from the Sun and the planet are balanced by the trojans' tendency to exit their orbit (Figure 1.2.b).
- *Centaurs Asteroids* have either a perihelion or a semi-major axis between Jupiter (5.209 AU) and Neptune (30.06 AU)
- *Trans-Neptunian Objects* orbit at a greater average distance than Neptune.

Group	Definition	
Atiras	$a < 1.0$ AU	$Q < 0.983$ AU
Atens	$a < 1.0$ AU	$Q > 0.983$ AU
Apollos	$a > 1.0$ AU	$q < 1.017$ AU
Amors	$a > 1.0$ AU	$1.017 < q < 1.3$ AU
PHA	$\text{MOID} \leq 0.05$ AU	$H \leq 22$

Table 1.1: Subclassification of NEAs, with a semi-major axis, Q aphelion distance, q perihelion distance, and H absolute magnitude.



(a) Comparison between a general NEA orbit and a PHA orbit.

Credits: NASA/JPL-Caltech

(b) Main asteroid belt and Trojan Asteroid.

Credits: Hubblesite

Figure 1.2: (a) Typical NEA and PHO
(b) Main Asteroid Belt and Trojan asteroids.

1.1.2 Composition-based classification

The composition of asteroids is various and poorly understood in most cases. However, an asteroid can be distinguished into three families according to the main elements by which it is composed:

- *C-type* (carbonaceous) asteroids, consisting of clay, minerals, and silicate rocks and dark in appearance. They are the most common and are thought to be the most ancient objects in the solar system.
- *S-type* (stony) asteroids, made up of silicate materials and nickel-iron.
- *M-type* (metallic) asteroids, mainly made of nickel-iron.

Each class has multiple subclasses, depending on the spectral appearance of the body. The asteroids' compositional differences are related to the distance from the Sun to which they formed.

1.2 The asteroid Bennu

On September 11, 1999, Bennu was discovered by the Lincoln Near-Earth Asteroid Research (LINEAR) during a NEA survey. Bennu is a B-type asteroid (a subtype of carbonaceous asteroids characterized by a blue spectral appearance), with an expected CM chondrite composition [24] (see Table 1.2). Bennu probably formed from a much larger carbon-rich asteroid in the Main Asteroid Belt at least 700 million years ago, and its present-day composition was already established within 10 million years of our solar system formation. Due to gravitational interactions with giant planets and the long-term Yarkovsky effect, the asteroid has wandered into near-Earth space.

Bennu (Figure 1.3), shaped like a spinning top, is classified as a NEO, specifically an Apollo asteroid, and meets the parameters to be considered a PHO, as it makes close approaches to Earth every six years, although its exact distance from Earth varies every time (see Table 1.3 for Bennu's main features). Bennu was chosen as the target of the OSIRIS-REx mission because it is considered a

potential time capsule of the birth of the Solar System, consisting of the original solar nebula matter. In particular, the availability of carbonaceous material, the basis of organic molecules necessary for life, was a determining factor in the choice. In the past, amino acids have been found in meteorites and comets, indicating that some ingredients necessary for life can be produced in space.

Despite the smooth homogenous material expected from telescope observations, the mission found a surface covered by rocks and boulders of various dimensions. Moreover, it was also discovered that Bennu ejects rocky particles into space. After analyzing data gathered during the sampling, it was clear that the spacecraft would have sunk into Bennu if it had tried to land on the surface to gather the material: the particles on Bennu's exterior are weakly bound together [47].

Temperatures on Bennu range from 116 °C to -73 °C and, because of the lack of atmospheric pressure, liquid water cannot exist on or under its surface.

Element	%	Element	%
H	1.15	Cl	0.05
C	2.32	K	0.04
N	0.11	Ca	1.20
O	42.41	Ti	0.06
Na	0.40	Cr	0.31
Mg	11.90	Mn	0.17
Al	1.14	Fe	21.10
Si	13.20	Co	0.06
P	0.10	Ni	1.25
S	3.00	Zn	0.02

Table 1.2: Bennu's expected composition as a CM chondrite [26].

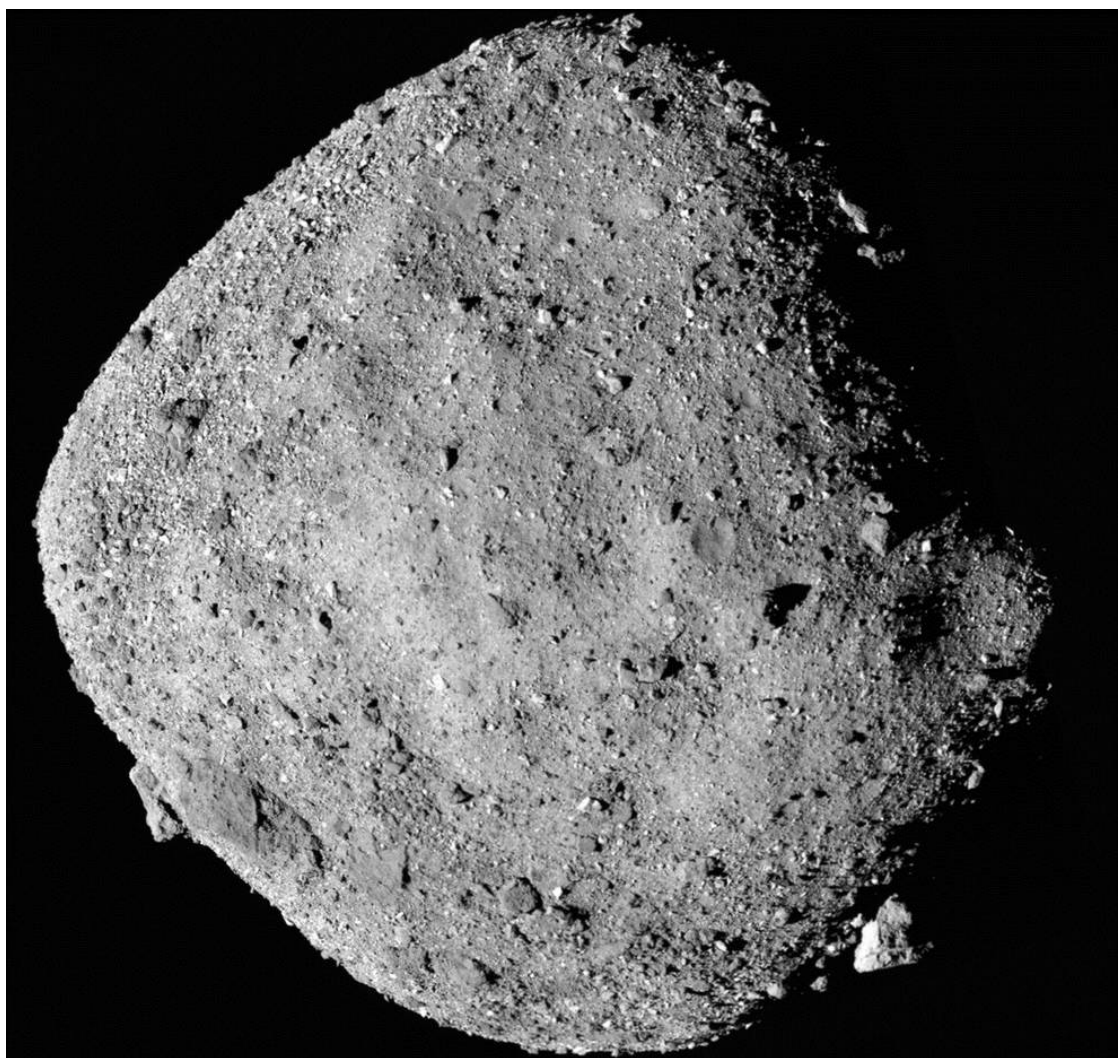


Figure 1.3: Image of Bennu collected by the OSIRIS-REx spacecraft from 24 km of distance.

Credits: NASA/Goddard/University of Arizona

i	6.0 °	T	1.12 y
e	0.20	a	1.13 AU
q	0.90 AU	Q	1.36 AU
MOID	0.003 AU	H	20.21
ρ	1.194 g cm ⁻³	d	482 m

Table 1.3: Bennu's orbital parameters and absolute magnitude, where i is the inclination of the orbit, T is the revolution period, e is the eccentricity, ρ is the average bulk density, and d is the average diameter.

1.3 Sample acquisition

In order to select the optimal sampling site for the mission, studies on the particle size-frequency distribution (PSFD) were carried out, aiming to find a location with a higher than-average abundance of surface particles less than 2 cm in diameter [12], ideal for the TAGSAM operations [22]. Larger particles would have compromised the collection process. In August 2019, the mission team chose four potential sampling sites: Nightingale, Kingfisher, Osprey, and Sandpiper (Figure 1.4), each situated within a crater with a high abundance of sampleable material. On December 12, 2019, Nightingale (located near the asteroid's north pole) and Osprey (near the equator) were selected as the primary and backup sample sites, respectively.

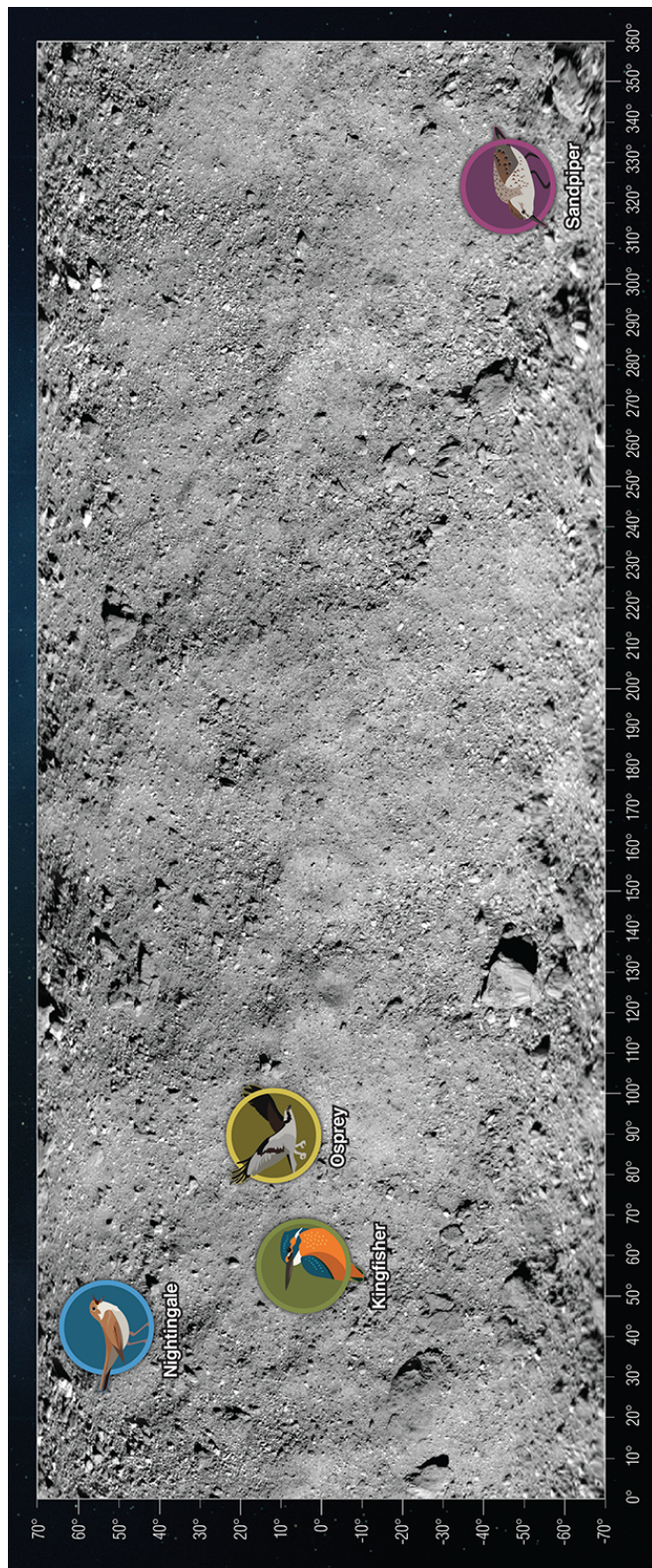
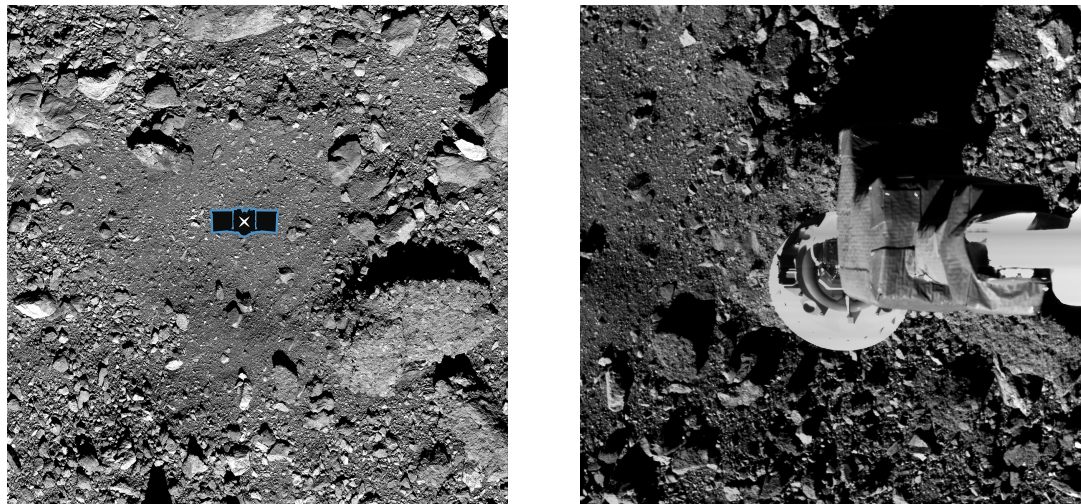


Figure 1.4: Projection of the candidate sampling sites' locations on the asteroid Bennu: Nightingale, Kingfisher, Osprey, and Sandpiper.
Credits: NASA/Goddard/University of Arizona

In October 2020, the OSIRIS-REx spacecraft left its orbit around the asteroid in order to collect the surface material (Figure 1.5). One second after contact with Bennu, TAGSAM, consisting of a circular collection device connected to the spacecraft by a mechanic arm, released nitrogen gas on the surface to channel the material in the collection chamber, penetrating 48.8 cm into the subsurface. The surface responded with minimal resistance to the contact of the spacecraft: the thrusters fired immediately to push the spacecraft back, not allowing it to sink into the loose soil.

SamCam and the TAGCAMS imager StowCam, two of the cameras installed on the spacecraft, showed that the acquisition mechanism was losing material, with an estimated amount of 55 g of particles leaving the collection chamber. Two days after the sampling, TAGSAM contained (317 ± 101) g of sample, but after six days the mass decreased to (250 ± 101) g, indicating a loss of 67 g.

Due to the high uncertainty of the sample mass, the amount of material that will be given to each laboratory is still unknown. Therefore, as explained in the next chapter, a systematic study of the sample geometry has been carried out for several masses in order to find a suitable solution for every possible sample mass.



(a) Hokioi crater, with the marker indicating the sampling area in panel (b).

Credits: <https://www.asteroidmission.org/candidate-sample-sites/nightingale/>

(b) TAGSAM contacting Bennu.
Credits: <https://www.asteroidmission.org/20200414samcamcheckpoint/>

Figure 1.5: Nightingale sampling site and sampling operations.

Chapter 2

Activity measurements at Monte dei Cappuccini Laboratory

Built in Turin in the early 1960s on the initiative of Prof. C. Castagnoli, the Monte dei Cappuccini Laboratory is the first underground laboratory in Italy, occupying a part of a former air-raid shelter (see the blue area in Figure 2.1). Since the 1990s, it has been dedicated to the study of meteorites [40][39] and the research in the paleoclimatology field. In 2002 underwent a radical restructuring with the employment of new equipment. Today, the laboratory is one of the best in the world for past solar activity studies based on meteorite analysis, and its management is currently being transferred from the National Institute of Astrophysics (INAF) to the University of Turin.

In this chapter, the γ -ray spectrometer that will be employed to analyze the sample is presented. The systematic study for the determination of the sample geometry is also described.

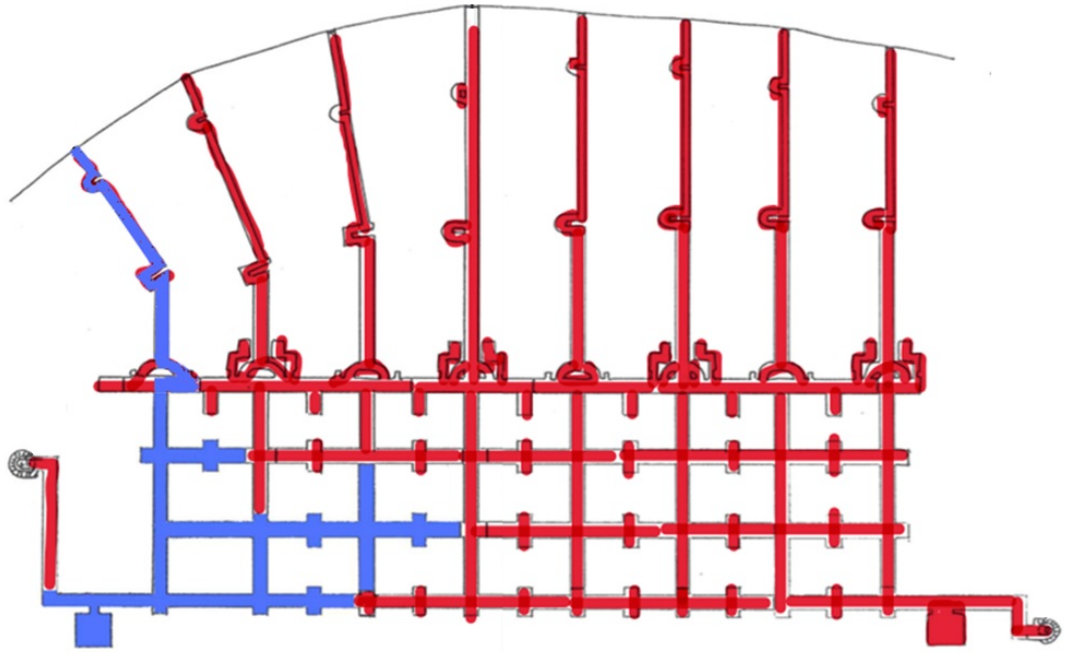


Figure 2.1: Floor plan of the Monte dei Cappuccini Laboratory. The tunnels of the air-raid shelter can be seen. The laboratory extends into the blue areas, with the entrance at the top left of the picture.

2.1 GEM 150 gamma-ray spectrometer

The laboratory has an effective shielding equivalent to 70 m of water that leads to a cosmic μ meson rate 30 times lower than at the surface [42][41]. The laboratory hosts two hyperpure germanium (HPGe) spectrometers: GEM 90 [9] and GEM 150 [39][14][15]. GEM 150 is a bigger and improved version of GEM 90 and will be employed for the measurement of the sample. Please refer to the respective references for a more detailed description of the spectrometers.

The GEM 150 consists of a 3 kg (cylindrical symmetry, 91.1 mm diameter x 89.2 mm length, 570 cm³ volume) p-type closed-ended coaxial HPGe (147% relative efficiency, 1.88 keV resolution, 104 peak-to-Compton ratio of for the 1332.5 keV of ⁶⁰Co γ -rays), surrounded by a 90 kg (23400 cm³) NaI(Tl) scintillator (see Figure 2.2). The system is located in a 20 cm thick low-activity lead shield with

an additional 5 cm thick OFHC (Oxygen-Free High-Conductivity) Cu-Cd-perspex graded shield for further background reduction and is cooled by liquid nitrogen (77 K). The cavity for the sample, which can host specimens up to 1.5 kg of mass, is continuously flooded with nitrogen gas to minimize the contribution of radon and its daughters, prevent humidity and avoid condensation. The HPGe detector operates in normal, coincidence, and anti-coincidence modes with the scintillator. In particular, the coincidence mode is set up to reduce the background by exploiting the particular radionuclide decays of interest. The detector signals are digitized by a multi-parametric acquisition system, allowing coincidence and anti-Compton spectroscopic analyses. The Ge background in the region of ^{22}Na peak at 1274.54 keV is (4.70 ± 0.15) cpd/keV, while in the region of ^{26}Al peak at 1808.65 keV it is (1.95 ± 0.09) cpd/keV. This system is suitable for detecting the feeble ^{44}Ti signal in meteorites fallen several centuries ago.

The NaI(Tl) inorganic scintillators can operate at environmental temperature but provide 10% energy resolution of the GEM150. They consist of a single annular crystal of 13.5 cm internal diameter, 10 cm thick, and 30 cm high, with six photomultipliers (PMTs). The internal cavity is closed on the top by a cylindrical plug (12.5 cm diameter, 10 cm height) with a seventh PMT.

A new electronic chain was purchased with funding from the Fondazione CRT and is being set up to optimize the acquisition of the detector signals.

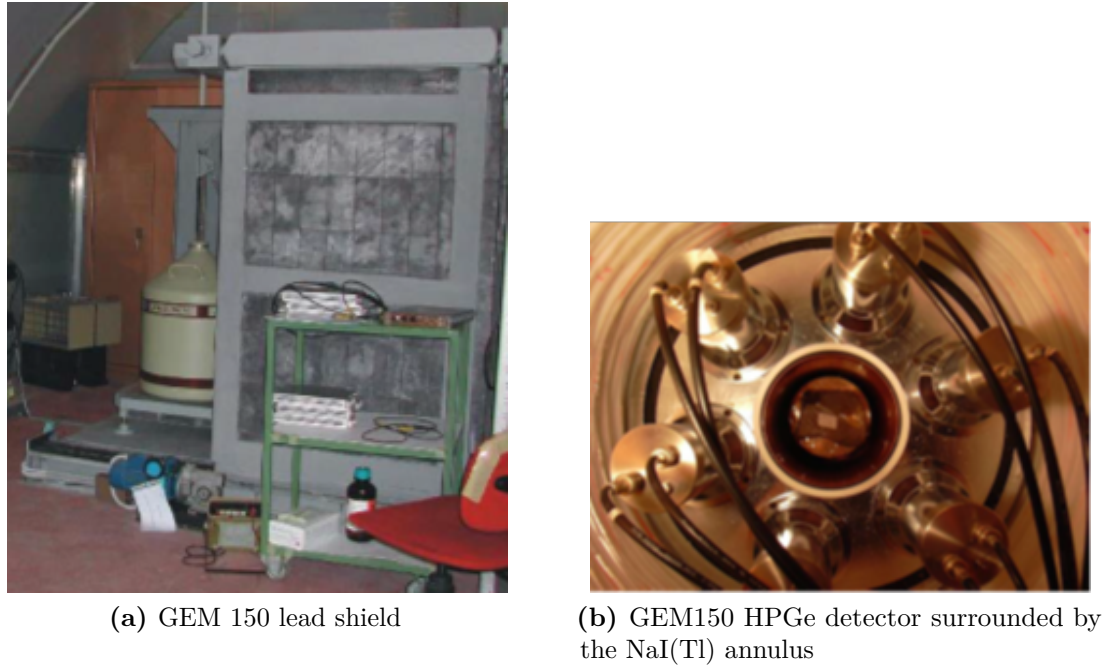
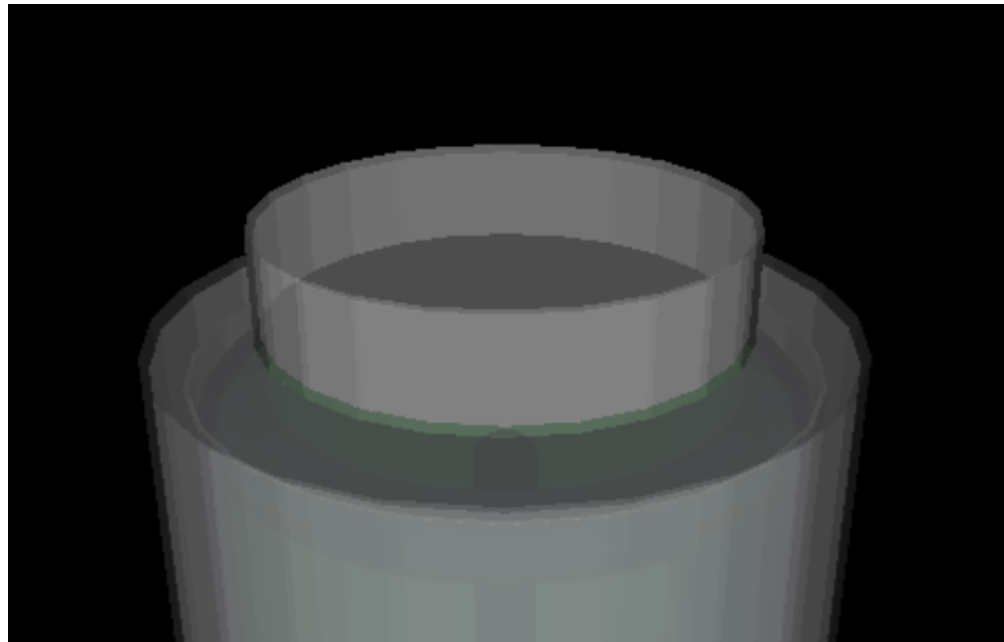


Figure 2.2: GEM 150

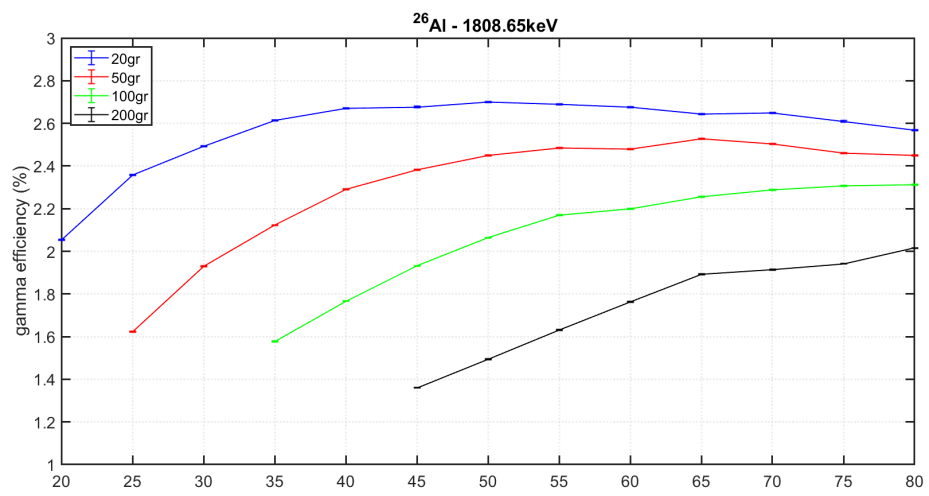
2.2 Study of the sample container

Due to the symmetry of the HPGe diode, a cylindrical shape represents the best to be measured. Thanks to a series of Geant4 simulations, systematic studies of the container dimensions were carried out in order to maximize the counting efficiency (for an introduction to the Geant4 toolkit, please refer to section 4.4).

In the model, the sample is placed in the cylindrical container on the detector, as shown in Figure 2.3.a. The decay of a known amount of ^{26}Al in the sample is simulated, and, by basing on the events actually detected by the HPGe, the counting efficiency of the apparatus is determined. As anticipated, a study on different possible masses from 20 g to 200 g was carried out and is shown in Figure 2.3.b: from 7 cm diameter on, the efficiency reaches a plateau and therefore, it has been chosen as the best dimension for the sample. Thus, the height of the container will vary according to the sample mass. The cylinder is meant to have a movable cover in order to adapt to the different possible masses.



(a) Cilyndrical container for the sample.



(b) Efficiency trend as a function of the container diameter.

Figure 2.3: Study of the sample container.

Chapter 3

Cosmogenic radionuclides in asteroids and meteorites

Solar activity is a multi-disciplinary topic, spanning from astrophysics to plasma dynamics and climatology. For the latter, studying the total solar irradiance variations is crucial for a better understanding of the Sun-Earth feedback mechanism.

It is widely known how the Maunder Minimum, the extraordinary solar irradiance minimum from 1645 to 1715, brought to the Little Ice Age, which had terrible consequences on the human population at the time. Similarly, but with less severe consequences, the Dalton Minimum between 1700 and 1800 brought a general lowering of the temperatures up to 1°C. Thus, predicting these variations is essential for the scientific and social improvements it represents.

The cosmic radiation flux is influenced by the heliospheric magnetic field (HMF), which is linked to solar activity. The reconstruction of the flux through the cosmogenic radionuclides activity measurements in celestial bodies allows for studying the Sun's magnetic field intensity in the past, which is crucial for the study of both the Sun's main modes of oscillation and the exposure history of the celestial body itself. The modulation of CRs due to solar activity leads to the modulation of the production of cosmogenic radionuclides; therefore, their activity reflects these variations. The study of nuclide decays with different half-lives allows for reconstructing the cosmic-rays exposure history of the studied body.

In this chapter, the concept of solar activity and its main modes of oscillation, the correlation between solar activity and CRs flux, and, therefore, between solar activity and cosmogenic radionuclides are briefly explained. The main parametrizations for the GCR flux are presented, which will be crucial for the cosmogenic radionuclides activity calculations.

3.1 Solar activity and its variations

Sunspots are dark, cold regions (4000 K compared to the 6000 K of the photosphere) visible on the Sun's surface, with a diameter ranging from 10^1 to 10^5 km, which led to the first observations of the variation of solar activity in the 17th century through studies of their number and dynamics on the solar disk. Galileo Galilei first observed sunspots in 1610 and published his "Lettere sulle macchie solari" in 1613, concluding that the Sun rotates for 27 days from East to West. Sunspots occur in two zones, north and south of the solar equator, with a maximum latitude of 29°, and are dragged along in the rotational motion. Only two centuries later, the differential rotation of the Sun was discovered by Lord Carrington. In 1826, the German astronomer S.H. Schwabe began recording the sunspot number (SN) he observed daily. After 17 years, the astronomer discovered in his data an 11-year periodic variation of the average SN, which became known as the Schwabe Cycle. The concepts of solar minimum and maximum are associated with this cycle. In 1958, Wolfgang Gleissberg published a paper describing an 87-year periodicity that modulates the Schwabe cycle, named the Gleissberg cycle after him.

Solar activity is strictly linked to solar wind and its properties. The existence of solar wind was postulated in 1951 by Biermann: from the observation of the angle between the dust tail and the plasma tail of comets, he concluded that the radiation pressure was not sufficient to explain the phenomenon, therefore implying the existence of a continuous flow of particles. In 1958 Parker proved the need for a stationary flow from the Sun (solar wind), associated with the impossibility of a static corona. Finally, the existence of the solar wind was definitively demonstrated by the Soviet probes Lunnik 2 and 3 (1960) and by Mariner 2 (1962).

Two different components of the wind can be identified at solar minimum:

fast (750 km/s), associated with the open magnetic field at polar zones, and slow (400 km/s), associated with the closed magnetic field at equatorial zones. At solar maximum, the two regimes are difficult to distinguish. The solar wind blows radially from the Sun and carries "freeze-in" with it the HMF, divided into hemispheres of opposite polarity by the heliospheric current sheet (CS), or interplanetary CS. The shape of the CS is the product of the influence of the Sun's rotating magnetic field on the plasma in the interplanetary medium, resulting in the so-called "ballerina skirt" shape, such as the Parker Spiral. The current sheet thickness is about 10^4 km near the orbit of the Earth.

The flux of cosmic rays, especially galactic cosmic rays, is modulated by the HMF, which is linked to the solar cycle: the magnetic field changes each polarity every 22 years: overall, the total solar cycle has a period of 22 years, called Hale cycle (two Schwabe cycles).

3.2 Cosmic Rays

Cosmic rays are high-energy ionized nuclei, electrons, neutrinos, and other particles that can originate from the Sun and outside of the Solar System and differ in composition, energy distribution, intensity, and temporal variations. The CR spectrum spans more than ten orders of magnitude in energy and thirty in flux, as shown in Figure 3.1.

A classification into three families due to their origin is possible: Solar Cosmic Rays ($E < 10^9$ eV), Galactic Cosmic Rays ($10^9 < E < 10^{17}$ eV), and Extra-Galactic Cosmic Rays ($E > 10^{17}$ eV), but the latter are often included in the galactic component. Supernovae are considered the sources of galactic cosmic rays, but much has yet to be revealed on this topic.

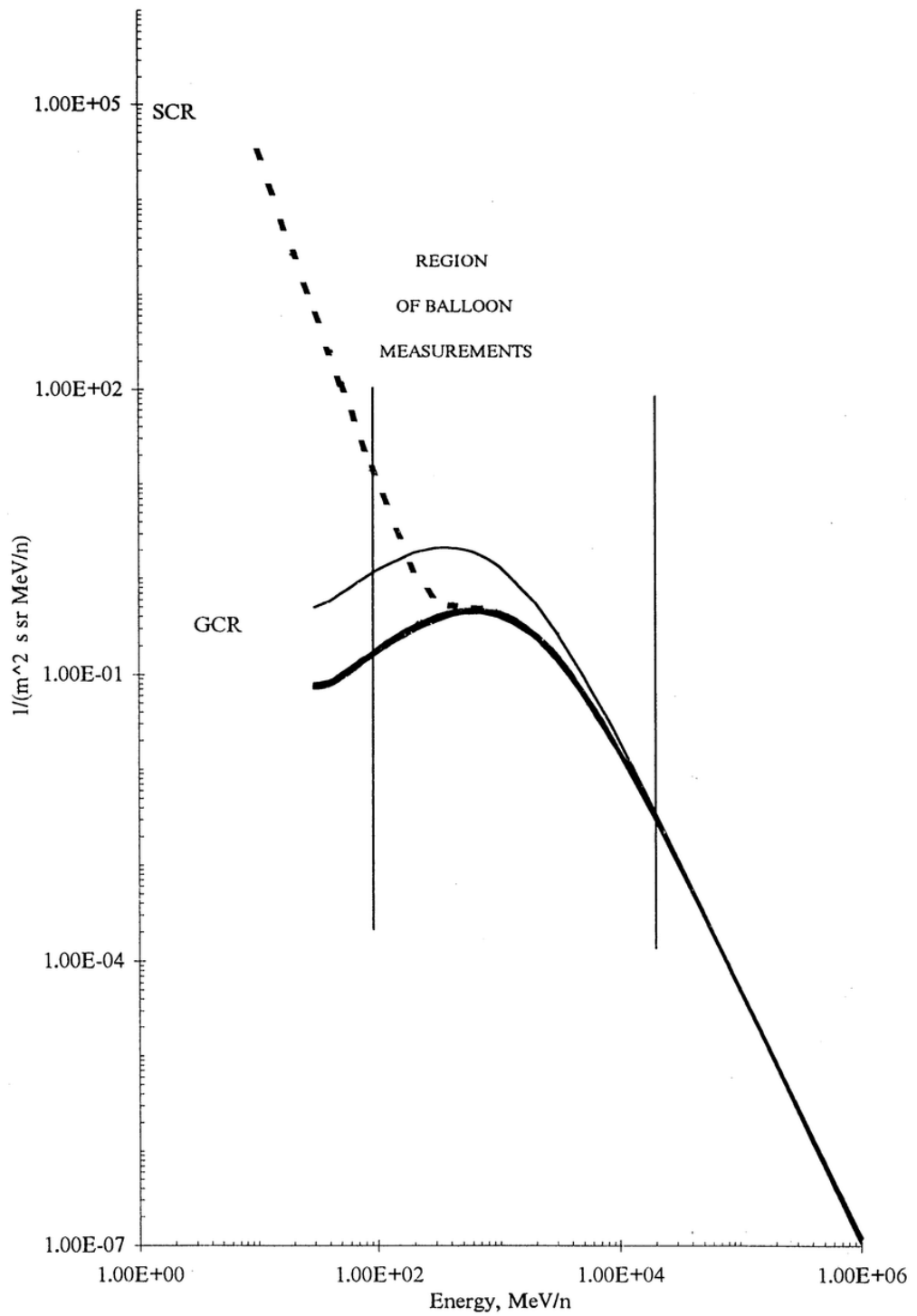


Figure 3.1: CR flux-energy spectrum from G.A. Bazilevskaya and A.K. Svirzhevskaya (1998) [5].

3.2.1 Solar Cosmic Rays (SCRs)

The Sun constantly emits a flux of particles through the solar wind. However, episodic high-energy solar activities, such as flares and coronal mass ejections (CMEs), increase the CR flux at energies below a few GeV with Solar Energetic Particles (SEPs). The emissions from these events are intrinsically different: solar flares provide impulsive acceleration, while the shock wave associated with a CME leads to a progressive acceleration. SEPs consist of 98% protons, 2% alpha particles [29], and a small number of heavier nuclei, traveling much faster than the ambient particles in the space plasma. Solar wind particles and SEPs represent the SCRs.

The average SCR flux is described as a function of the rigidity ϕ [29]:

$$J_{SCR} = J_{0,SCR} \cdot e^{-\frac{\phi}{\phi_0}} \quad (3.1)$$

with a characteristic rigidity ϕ_0 in MV units and $J_{0,SCR}$ in particles/(m² sr s MeV/nucleon) units.

3.2.2 Galactic Cosmic Rays (GCRs)

Galactic Cosmic Rays are atomic nuclei completely ionized during the acceleration outside our solar system, reaching relativistic speed. Their average composition is about 87% protons, 12% alpha particles, and less than 1% of heavier nuclei, but these concentrations vary with time and energy. When entering the heliosphere, GCR particles interact with the HMF, leading to scattering, diffusion, energy loss, and the modulation of the particle energy spectra, especially below 10 GeV. Studies of the temporal variations of the cosmic-ray flux, based on long-lived cosmogenic nuclides in meteorites and lunar samples, allow for concluding that the long-term average galactic cosmic ray flux is essentially constant in the past 10⁴-10⁷ years [21].

3.2.3 GCR flux parametrizations

Many models of the GCR production and propagation have been developed, and most of them are based on the numerical solution of Parker's cosmic-ray transport equation (1965) [31]. The time-dependent differential energy spectrum of a GCR component can be parameterized by the so-called "force-field" approximation, which assumes azimuthal and spherical symmetry:

$$J(E, M) = J_{LIS}(E + M) \cdot \frac{E(E + 2mc^2)}{(E + M)(E + M + 2mc^2)} \quad (3.2)$$

where m is the particle mass, E is the kinetic energy per nucleon, and M is the particle-related modulation parameter, which will be described later. This parametrization depends on the local interstellar spectrum J_{LIS} , such as the galactic particle spectrum outside the heliosphere. There are many expressions for this term that mainly differ from each other at low energies (< 10 GeV) [25]. One of these expressions, useful for later explanations, is given by Burger et al. (2000) [11]:

$$J_{LIS,BG}(E) = 1.9 \cdot 10^4 \cdot \frac{P(E)^{-2.78}}{1 + 0.4866P(E)^{-2.51}} \quad (3.3)$$

where

$$P(E) = \sqrt{E(E + 2mc^2)} \quad (3.4)$$

is the particle rigidity.

E is expressed in GeV/nucleon units, while J_{LIS} is expressed in particles/(m² sr s GeV/nucleon) units. Most cosmogenic radionuclides studies, including this thesis, are based on Castagnoli and Lal's LIS parametrization (1980) [13] as follows:

$$J_{LIS,CL}(E) = 9.9 \cdot 10^8 \cdot (E + 780 \cdot x) \quad (3.5)$$

where x is parameterized as

$$x = e^{-2.4 \cdot 10^4 \cdot E} \quad (3.6)$$

In this case, E is in MeV/nucleon units and J_{LIS} is expressed in particles/(m² sr s MeV/nucleon) units.

In Figure 3.2, the differences between Burger's and Castagnoli's parametrizations for protons are shown. A modulation parameter equal to 660 MeV has been chosen, such as the mean value observed from Earth from ^{26}Al activity studies [25].

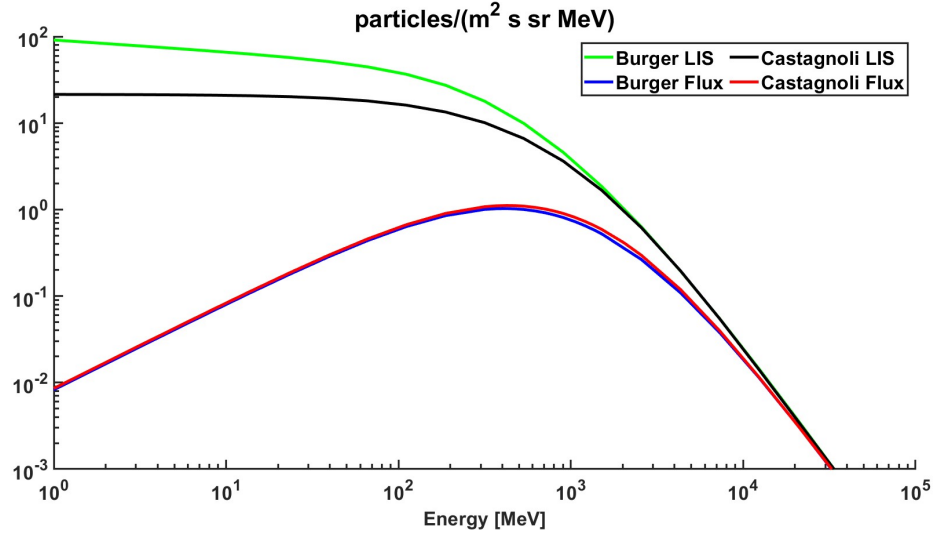


Figure 3.2: Burger parametrization vs Castagnoli parametrization. The high-energies limit leads to the same values for both modulated and unmodulated LIS. As expected, high-energy particles are not influenced by the interplanetary magnetic field.

For alpha particles, Leya et al. (2021) [25] introduced a new parametrization specifically for the cosmogenic radionuclides production calculation as follows (see Figure 3.3 for the comparison with protons):

$$J_\alpha(E) = 5.5 \cdot 10^7 \cdot \frac{E^k(E + 2m_\alpha c^2)}{(E + 700)(E + 2m_\alpha + 700)(E + 312500E^{-2.5} + 700)^{1.65+k}} \quad (3.7)$$

where m_α is the mass of the helium nucleus, E is the energy in MeV/nucleon units, and the flux is expressed, as for Castagnoli's parametrization, in $\text{particles}/(\text{m}^2 \text{ sr s MeV/nucleon})$ units. The parameter k is expressed as

$$k = 3.572 M_\alpha \cdot 10^{-3} - 0.1323 \quad (3.8)$$

where M_α is the modulation parameter of alpha particles. See the following subsection for clarification on the modulation parameter dependence on the particle type.

Note that this equation should only be considered a model for the radionuclides production evaluation. It is not derived by heliospheric transport and modulation calculations.

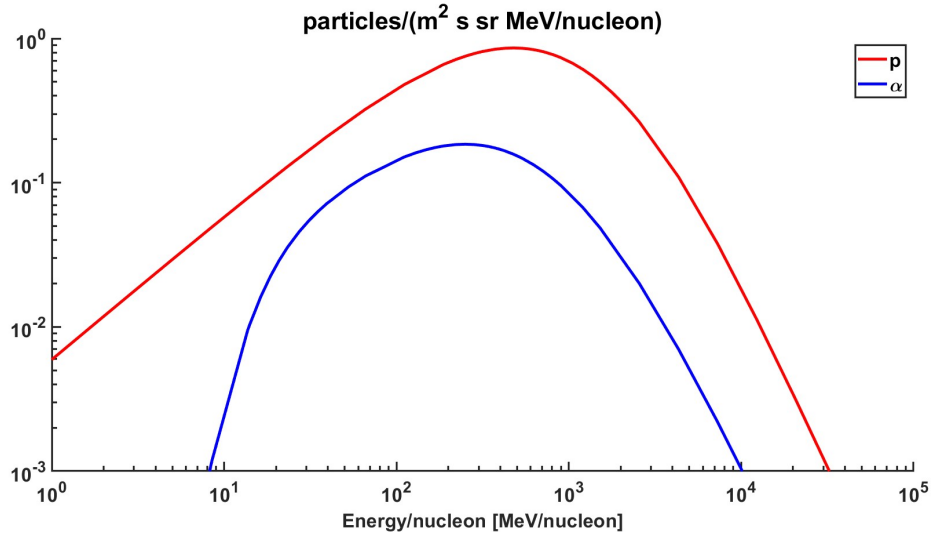


Figure 3.3: Leya's α parametrization vs Castagnoli's proton parametrization with a 660 MeV and a 330 MeV modulation parameters for protons and α -particles, respectively. In the next subsection, the fact that these two values correspond to the same solar activity intensity will be clear.

3.2.4 Modulation parameter

The modulation parameter M can be interpreted as the mean adiabatic energy loss for a galactic particle that enters the heliosphere, however, it does not have real physical meaning, and it is implemented in the flux parametrization in order to consider Sun's influence on the particle energy spectrum. It can be calculated as

$$M = \phi \frac{eZ}{A} \quad (3.9)$$

where e is the elementary charge and ϕ , Z , and A are, respectively, the rigidity,

the atomic number, and the atomic mass of the particle. This means that M_α is half the modulation parameter for protons, as introduced in Figure 3.3.

Strictly speaking, a dependence on time and distance from the Sun should be implemented in equation 3.9 since the rigidity ϕ is correlated to the solar magnetic field, which has its typical variations. Therefore, the GCR flux intensity indirectly gives information about the heliospheric magnetic field through the modulation parameter.

With equal solar activity, the modulation parameters for Castagnoli's and Burger's functions are different and are linked with a simple expression [25]:

$$M_{CL} = 0.97 \cdot M_{BG} - 78 \text{ MeV} \quad (3.10)$$

For future considerations, note that modulation parameters from the Usoskin's series [46], which considers Burger's expression, and Castagnoli's flux parameterizations will be employed. Thus, the modulation parameter values must always be intended as converted from M_{BG} to M_{CL} for the calculations.

In Figure 3.4 the anti-correlation between the modulation parameter and Castagnoli's parametrization of the proton flux is shown. Once again, the high energies limit gives the same result independently from the value of M . As expected, high-energy particles are not considerably influenced but the solar magnetic field. These results agree with BESS and PAMELA experiments, as shown in Figure 3.5.

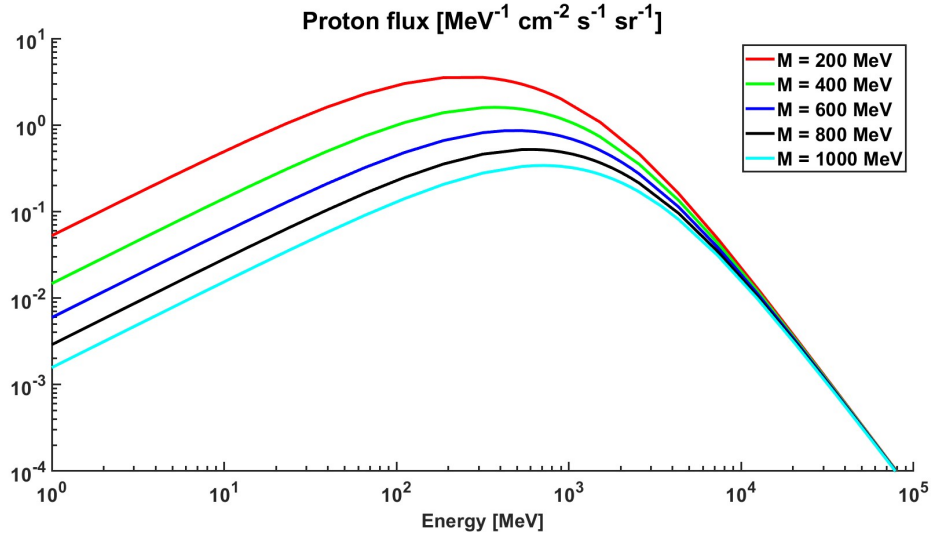


Figure 3.4: Castagnoli's parametrization for 5 modulation parameters values, from 200 to 1000 MeV.

A correlation should be visible from the sunspot number and modulation parameter series. In Figure 3.6, the monthly mean sunspot number series from International Sunspot Number (ISN) series and the reconstructed monthly mean modulation parameter series [46] are shown from 1936 to 2009.

A simple covariance coefficient can be calculated between the two series with expressions 3.11 and 3.12. The calculation has been performed with the yearly average values of both variables in order to avoid high-frequency variations:

$$r_{M,SN}(l) = \sum_{y=1936}^{2009} [M(y) - \bar{M}][SN(y-l) - \bar{SN}] \quad (3.11)$$

$$\rho(l) = \frac{r_{M,SN}(l)}{\sqrt{r_{SN,SN}(0) \cdot r_{SN,SN}(0)}} \quad (3.12)$$

where l is the lag, and the barred terms are the mean values of the respective series. The normalization consists in the square root of the two auto-covariances at zero lag. In Figure 3.7 the result can be seen. The deep correlation between the sunspot number, which represents the level of solar activity, and the modulation parameter of the GCR flux highlights the capability of reconstructing the solar

activity through the GCR flux and vice versa.

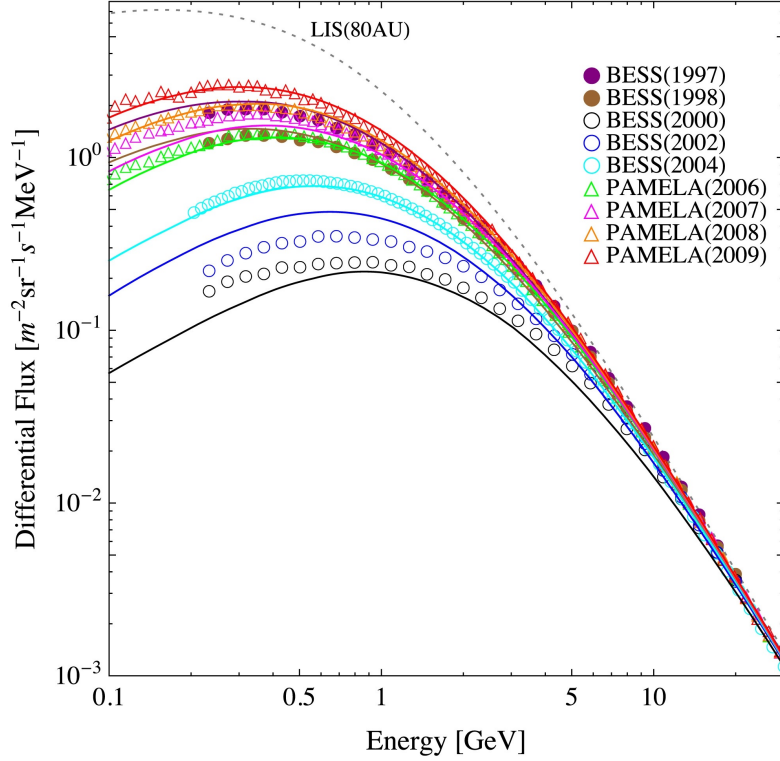


Figure 3.5: BESS and PAMELA experimental results (points), which can be represented by the force-free approximation (continuous lines). The data from 1997 to 2009 allow for highlighting the GCR flux variation during a complete 11-year cycle. By following the chronological order of the data on the graph, it is easy to note the initial diminution of the flux intensity from 1997 to 2002 and then the ascent from 2004 to 2009. Figure adapted from Miyake, S., R. Kataoka, and T. Sato, (2017) [30].

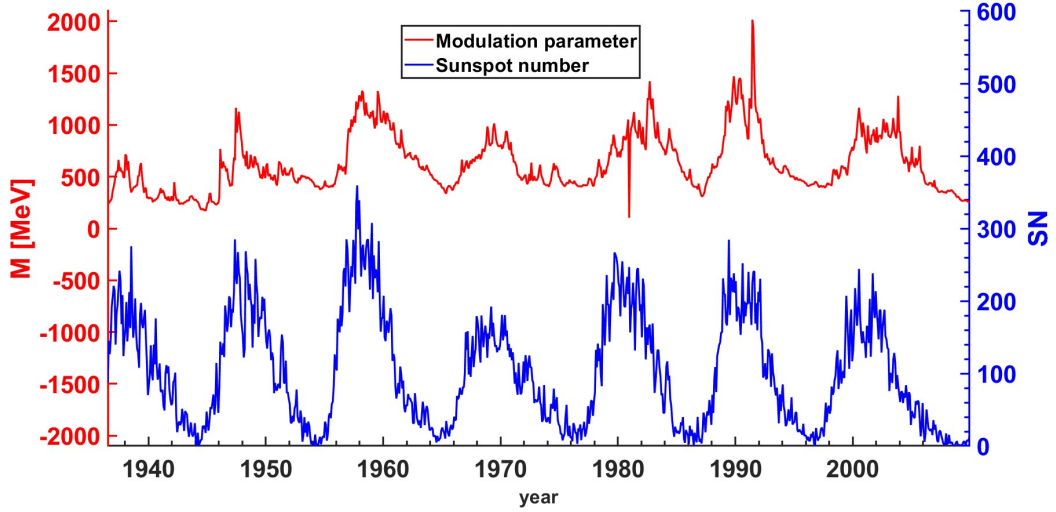


Figure 3.6: Monthly mean sunspot number (blue) and modulation parameter (red) compared. It is clear from this image that a general correlation exists between the two series, both strictly linked to solar activity.

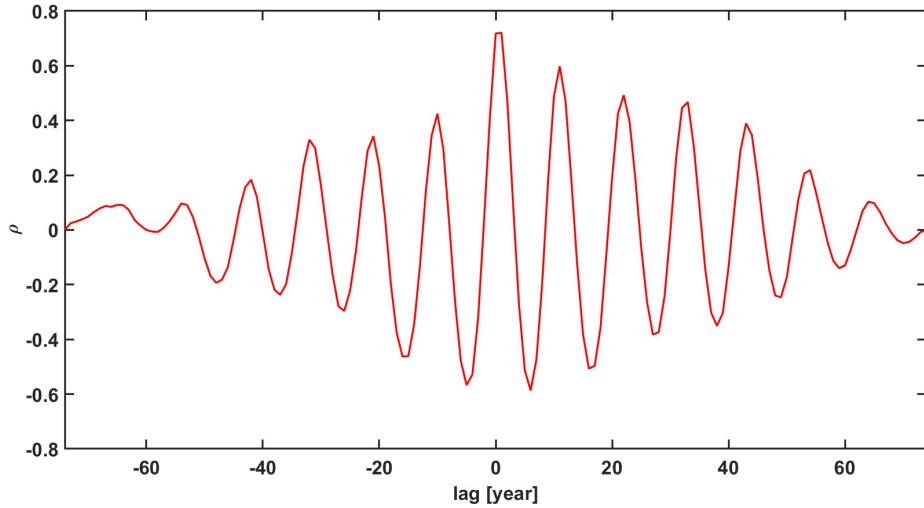


Figure 3.7: Covariance coefficient between yearly average sunspot number and reconstructed modulation parameter. We have a 0.7 coefficient with zero lag, which implies a high correlation between the two series. Moreover, we can see from non-zero lags that the strong oscillation reveals the presence of the dominant decadal cycle.

3.3 Cosmogenic radioisotopes

Cosmogenic isotopes are the interaction (spallation, neutron capture, etc.) products of the hadronic component of cosmic rays impacting the interstellar matter, in particular Earth's atmosphere, meteorites, and asteroids [6]. An example of spallation is a proton colliding with a ^{16}O nucleus in Earth's atmosphere, which yields two protons, a neutron, an alpha particle, and a radioactive ^{10}Be nucleus, that decays into ^{10}B after $1.4 \cdot 10^6$ years on average.

Cosmogenic radionuclides represent a perfect tool for studying the GCR flux in the past and therefore reconstructing the solar activity through the modulation parameter. In terrestrial reservoirs, cosmogenic radionuclides concentrations are affected by geomagnetic shielding and climatic changes, which mainly result in deposition rate and global mixing variations within the different reservoirs and lead to a biased reconstruction of the GCR flux. A solution to this problem is measuring the radioactivity of bodies not influenced by these phenomena, such as asteroids and meteorites. Investigating cosmogenic nuclides in extraterrestrial matter allows for studying the CR exposure history of the matter itself and the CR spectral distribution over time scales of millions of years.

Celestial bodies are exposed to both SCRs and GCRs, resulting in the production of several cosmogenic isotopes. The production rate of a nuclide depends on the fluxes of primary (cosmic ray) and secondary (product of the interaction of primaries in the matter) particle fluxes. The measurement of cosmogenic radionuclides reveals the exposure history of the body during a period of about three half-lives of the radioisotopes. Therefore, measuring radioisotopes with different half-lives represents a method to study the GCR flux at different timescales. ^{22}Na , with a half-life of 2.6 years, and ^{54}Mn , with a half-life of 312 days, can be considered suitable for identifying the 11-year cycle-related GCR flux variations [40]. On the other hand, the Gleissberg cycle must be studied by measuring the radioactivity of an isotope with a half-life value between 11 years and 87 years since it must be influenced just by the longer modulation. The best candidate is found in the ^{44}Ti , with a half-life of 59 years [39][43][4][45]. Long-lived radioisotopes can be useful to determine the mean GCR flux over a time-lapse much longer than the known Sun's periodicities, such as one million years. ^{26}Al turns out to be the best candidate

for this purpose because it is largely produced in the interstellar matter and has a half-life of $7.2 \cdot 10^5$ years.

3.3.1 Production and secular equilibrium

The variation with time of the number N of radioactive atoms at a given depth can be expressed as:

$$\frac{dN}{dt} = P(t) - A(t) = P(t) - \lambda N(t) \quad (3.13)$$

where P is the production rate due to CRs and A is the element's activity, which is given by the product between the number of radionuclides and the decay constant. Resolving this differential equation is complicated due to the fact that the correct expression of $P(t)$ is difficult to determine as it depends on the Sun's activity variabilities. For long-lived radionuclides like ^{26}Al , $P(t)$ can be considered constant because short-time variations of the irradiation do not influence it. In this way, equation 3.13 becomes a simple separable differential equation:

$$\int_{N_0}^N \frac{dN}{P(t) - \lambda N(t)} = \int_{t_0}^t dt \quad (3.14)$$

where, for the sake of simplicity, the upper extremes of integration are the same as the variable of integration. This leads to:

$$N(t) = \left(N_0 - \frac{P_0}{\lambda} \right) e^{-\lambda t} + \frac{P_0}{\lambda} \quad (3.15)$$

Since the considered radionuclides are purely cosmogenic, we can assume that at $t_0 = 0$, such as the time at which the exposition to the radiation began, there are no nuclei of those elements ($N_0 = 0$). Finally, by multiplying with λ , we obtain the activity as a function of time:

$$A(t) = P_0 (1 - e^{-\lambda t}) = P_0 (1 - e^{-\frac{t}{\tau}}) \quad (3.16)$$

where $\tau = \frac{1}{\lambda}$ is the half-life of the nucleus. Assuming the secular equilibrium, such as an exposition time t such that $\frac{t}{\tau} \sim \infty$, the activity reaches its asymptotic value

equal to P_0 . In Figure 3.8, the trend of equation 3.16 normalized to P_0 can be seen.

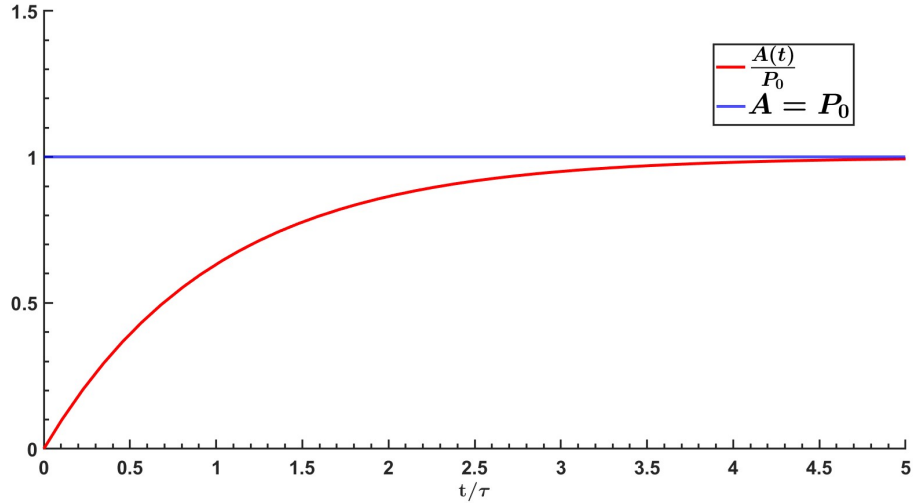


Figure 3.8: Saturation trend of the activity of a radionuclide with constant production rate. The x-axis is expressed in τ units, and the asymptote indicates the attainment of secular equilibrium, for which activity is equal to the rate of production.

To deduce the theoretical production rate in Bennu, the secular equilibrium is assumed. Due to its CM chondrite-like composition (Table 1.2), the expected radionuclides to be detected in Bennu are ^{26}Al , ^{44}Ti , ^{60}Co , ^{22}Na , ^{54}Mn , and ^{57}Co (see Table 3.1 for their properties). Since only ^{26}Al has a half-life such that the secular equilibrium with a constant production is possible, some considerations must be made in order to determine the activities of the other nuclides correctly. In subsection 4.4.3, a solution to this problem is proposed.

Nuclide	Half-life	Production	Main target elements
^{26}Al	$7.2 \cdot 10^5$ y	spallation	Mg, Al, Si, Ca, Ti, Fe, Ni
^{44}Ti	59 y	spallation	Ti, Fe, Ni
^{60}Co	5.3 y	neutron capture	Co
^{22}Na	2.6 y	spallation	Mg, Al, Si, Ca, Ti, Fe, Ni
^{54}Mn	312 d	spallation	Fe, Ni, Mn
^{57}Co	272 d	spallation	Fe, Ni

Table 3.1: Expected radionuclides in Bennu’s surface sample. The half-lives are updated to Kondev et al. (2021) [20].

3.3.2 $^{22}\text{Na}/^{26}\text{Al}$ activity ratio

^{22}Na and ^{26}Al are some of the most common radioisotopes in asteroids and meteorites and are produced by the same target elements through spallation. This property implies that the ratio between the GCR-induced radioactivities of the two nuclides is independent of the size of the body and the depth to which the activities are measured. Thus, the $^{22}\text{Na}/^{26}\text{Al}$ activity ratios can be compared between different bodies with similar compositions. This method is used in climatology for studying the Schwabe cycle and will be important in this work, as explained in the next chapter.

The expected $^{22}\text{Na}/^{26}\text{Al}$ activity ratio trend in the past can be calculated through the ISN series. The modulation parameter, which is anti-correlated to the GCR flux as already seen in Figure 3.4, is characterized by the same periodicities as the number of sunspots (see the previous Figures 3.6 and 3.7). Therefore, the $^{22}\text{Na}/^{26}\text{Al}$ ratio trend in the past can be derived by applying the opposite oscillation of the SN to the mean value of the ratio. However, attention must be paid to the fact that a radionuclide activity is influenced by the GCR flux of the previous 2-3 half-lives: this feature must be implemented in this calculation. The solution is found by applying the following method. Note that the monthly SN series is

employed in this case.

First, the opposite periodicity must be obtained from the SN series. This is done by determining the so-called "reversed" sunspot number series, where i is the index ranging from 1 to the length of the series and $\max(SN)$ is the maximum value of the series.

$$SN_{REV}[i] = \max(SN) - SN[i] \quad (3.17)$$

Now, the support series S is introduced.

$$S[n] = \sum_{i=1}^n SN_{REV}[i] \cdot e^{-\lambda(t_n - t_i)} \quad (3.18)$$

where the sum is weighted by the radioactive decay exponential law of the considered nucleus. This is useful to implement the dependence of the radioactivity on the GCR flux history. The exponential decrease weights the influence of the past activity, with a zero influence at minus infinity time, as expected.

Finally, the ratio is calculated:

$$\frac{Na}{Al}[n] = \overline{\frac{Na}{Al}} \cdot \frac{S[n]}{\overline{S}} \quad (3.19)$$

where the barred term is the mean value of the series. Now, the result lies in determining the average ratio and the support series.

For Bennu, we calculated the average $^{22}\text{Na}/^{26}\text{Al}$ ratio with Reedy and Arnold's model (1972) [35], obtaining 1.7, and we drew the expected ratio trend over the past years (Figure 3.9). A delay of about two years is related to the half-life of the radioisotope.

Thanks to this approach, we were able to determine a value of the ratio equal to 2.1 for October 2020, such as the month of sample extraction. As explained in the next chapter, this will be useful for calculating the production rates trend.

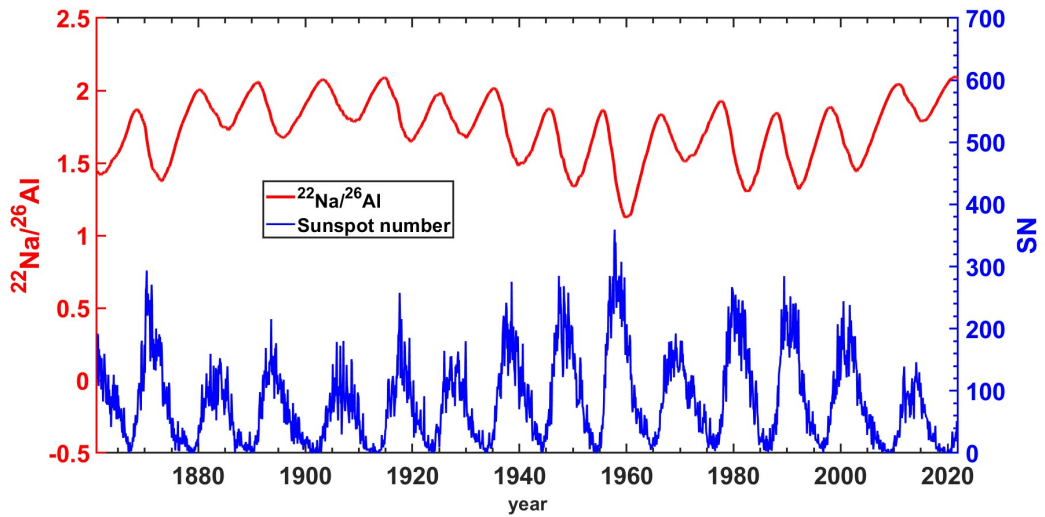


Figure 3.9: Expected $^{22}\text{Na}/^{26}\text{Al}$ radioactivity ratio in Bennu in the past 150 years compared to the SN series. The same results for H and L chondrites can be seen in Taricco et al. (2010) [40].

In the next chapter, the radionuclides production models used for the expected radioactivity estimations are described.

Chapter 4

Cosmogenic radionuclides production models

The production of cosmogenic nuclides in an asteroid at a given depth depends on the size and bulk chemical composition of the body and the CR flux intensity. The production rate P_i of a cosmogenic isotope i by the interaction of the component x of the CR flux at the given depth in the interstellar matter is calculated as the sum of the production rates by SCRs and GCRs:

$$P_{i,x} = P_{SCR,i,x} + P_{GCR,i,x} \quad (4.1)$$

The total production of the isotope is given by the sum of all the significant components of the flux:

$$P_i = P_{i,pp} + P_{i,sp} + P_{i,sn} + P_{i,p\alpha} \quad (4.2)$$

where pp and $p\alpha$ are, respectively, the primary protons and alphas, while sp and sn are secondary protons and neutrons. Note that the presence of neutrons in the primary flux and α -particles in the secondary flux can be neglected.

Secondary particles, especially neutrons, are produced in significant amounts by the interactions of the galactic primaries and dominate the production at high depths [25][27][29]. Therefore, the depth-dependent particle flux takes into account both primary and secondary spectra.

Due to their low energies, SCR primaries produce only negligible amounts of secondary particles, which can be neglected for SCR calculations with a good level of approximations. Moreover, solar helium nuclei can also be ignored because of their low abundance.

The expression of the production rate $P_{i,x}$ is given by:

$$P_i(R, d, c_s, c_b, M) = N_A \sum_{j,x} \frac{c_{s,j}}{A_j} \int \sigma_{i,j,x}(E_x) \cdot J_x(E_x, R, d, c_b, M) dE_x \quad (4.3)$$

In the next table (Table 4.1), the parameters in the equation are explained.

Parameter	Definition
R	meteorite radius
d	depth
c_s	chemical abundances vector of target elements
c_b	bulk chemical composition
M	modulation parameter
N_A	Avogadro's number
A_j	mass number of the target element j
$\sigma_{i,j,x}$	cross-section of the production of isotope i by the interaction between component x of the flux and target element j
E_x	energy of the component x of the flux
J_x	flux of the component x at depth d

Table 4.1: Parameters of the production rate equation 4.3.

Note that this formula is associated with Michel et al. (1991) [27] physical model for the production rates. This model will be discussed later but can also be considered as the theoretical equation describing the actual physics of the phenomenon. Equation 4.3 states that all the CR energy spectrum, weighted by the energy-dependant cross-section of the specific interaction taken into account, contributes to the production of a cosmogenic radionuclide. The complexity of resolving this equation lies precisely in the cross-section and depth-dependent flux expressions. Therefore, many empirical and semi-empirical models have been proposed over time (see Reedy and Arnold (1972) [35] and Bhandari and Podtar (1982) [7] as an example).

4.1 SCR production

Due to their low energies, SCR-related radionuclide production is limited to shallow depth scales, such as the outer surfaces of the irradiated object. The maximum relevant depth for SCR interactions is of the order of magnitude of 10 g cm^{-2} . Production rates due to secondary SCR particles are negligible and therefore are not included in the transport code calculations.

In Figure 4.1 the results from Reedy and Arnold semi-empirical model [35] for ^{26}Al and ^{22}Na are shown. The rigidities of the flare spectra range between 20 MV and 150 MV. In this thesis, 125 MV rigidity was taken into account for SCRs.

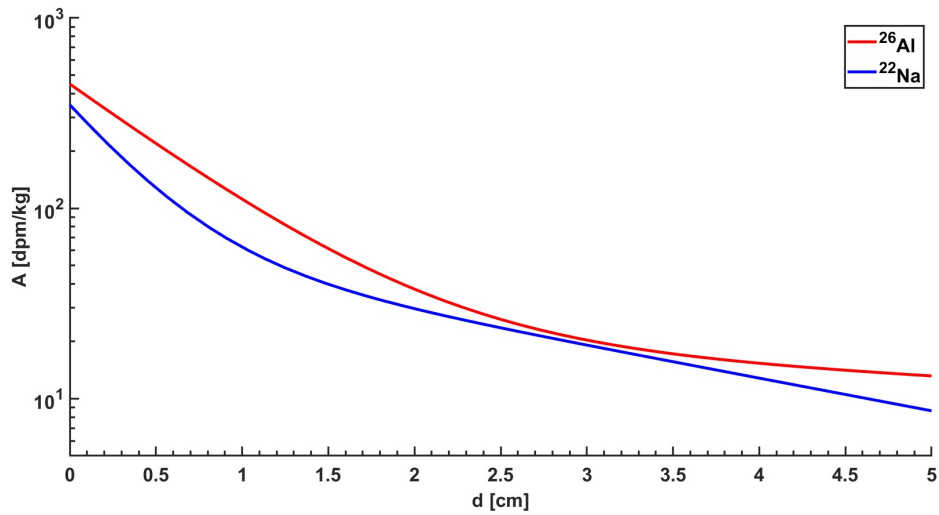


Figure 4.1: ^{26}Al and ^{22}Na SCR-induced radioactivities up to 5 cm of depth.

4.2 GCR production - physical model

In 1991, Michel et al. proposed a physical model for the calculation of the GCR-induced radioactivity based on the numerical resolution of equation 4.3 through Monte Carlo methods [27]. The core of this method is the determination of the particle flux at each depth step with the stochastic approach. The depth and size-dependent spectra of primary and secondary particles are calculated by Monte Carlo codes such as HETC or LAHET for high-energies protons and neutrons, coupled with MORSE or MCNP for low-energy neutrons, which can as well lead to nuclear interactions [29].

With this model, we calculated the activity of ^{26}Al in Bennu and then we determined ^{22}Na activity through the $^{22}\text{Na}/^{26}\text{Al}$ ratio, as explained in the subsection 3.3.2. The expected ratio in the month of sampling is equal to 2.1.

The order of magnitude of the depth scale on which GCR interactions occur is 100 g cm^{-2} , meaning that GCR production dominates at high depths over SCR production.

Although α -particles are completely neglected in the SCR calculations, they must be taken into account for GCR-induced productions. Instead of directly

calculating production rates due to helium nuclei, a different approach is often applied. Since the average composition of GCRs is 87% primary protons and 12% alpha particles, for each primary proton there are 0.138 primary α -particles. Since each α has four nucleons, there are 0.55 primary α -nucleons for each proton. Assuming that each nucleon leads to the same production as a single proton, the production rate due to alpha particles can be calculated as [28]:

$$P_{p\alpha} = 0.55 \cdot P_{pp} \quad (4.4)$$

Note that this method is discussed today, and a new approach with a Geant4 simulation is described in section 4.4.

In Figure 4.2 the results for ^{26}Al and ^{22}Na are shown up to 50 cm. In this case, the calculation for Bennu was executed assuming an infinite radius for the asteroid, such as a flat surface on which the CRs impact.

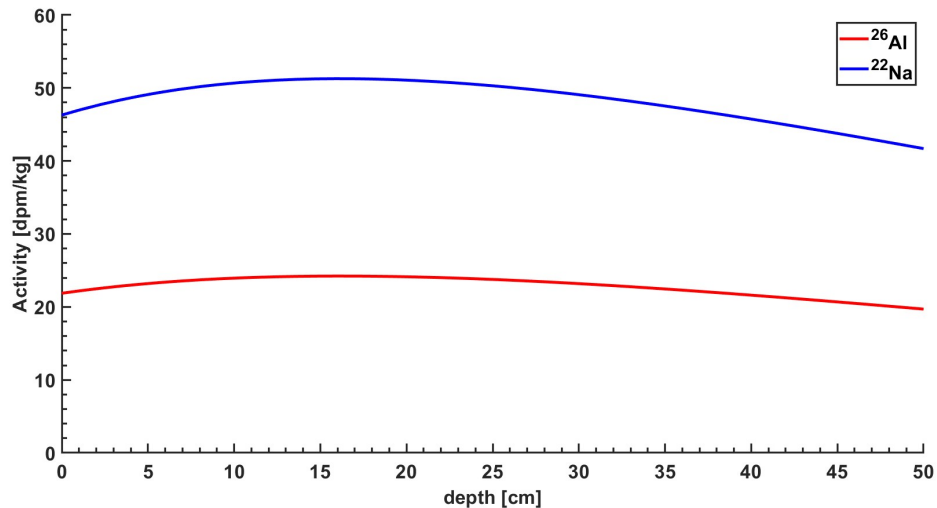
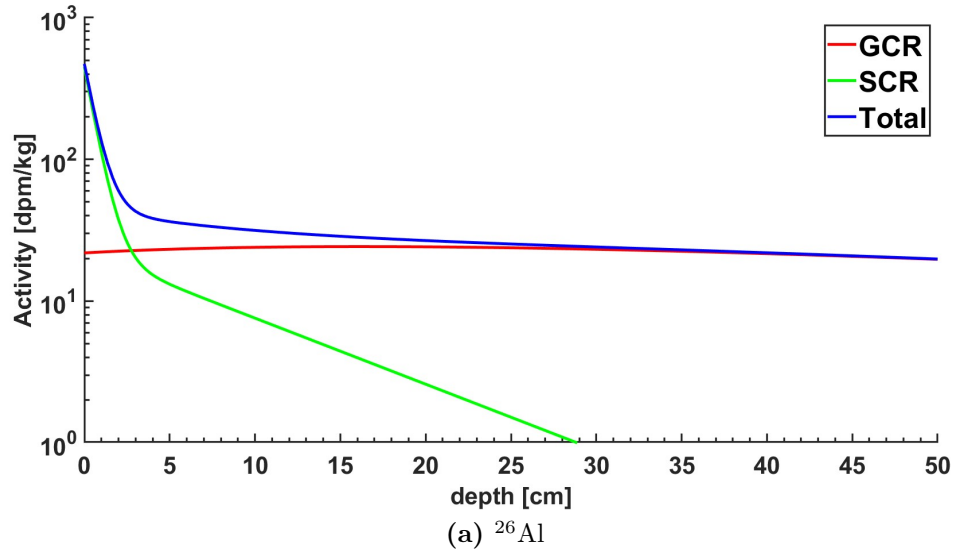


Figure 4.2: ^{26}Al and ^{22}Na GCR-induced radioactivities up to 50 cm of depth.

4.3 Total production

As explained by equation 4.1, the total production is given by the sum of the SCR and GCR productions (Figure 4.4). The total trend is a monotonically decreasing function; therefore, there is a bi-univocal correspondence between the mean value over the range $[0, \text{depth}]$ and the considered depth. Thanks to this property, the depth of the surface sample can be indirectly deduced by the radioactivity measurements. In Chapter 5, thanks to the total activity in Bennu, we estimated the expected radioactivity of the sample.



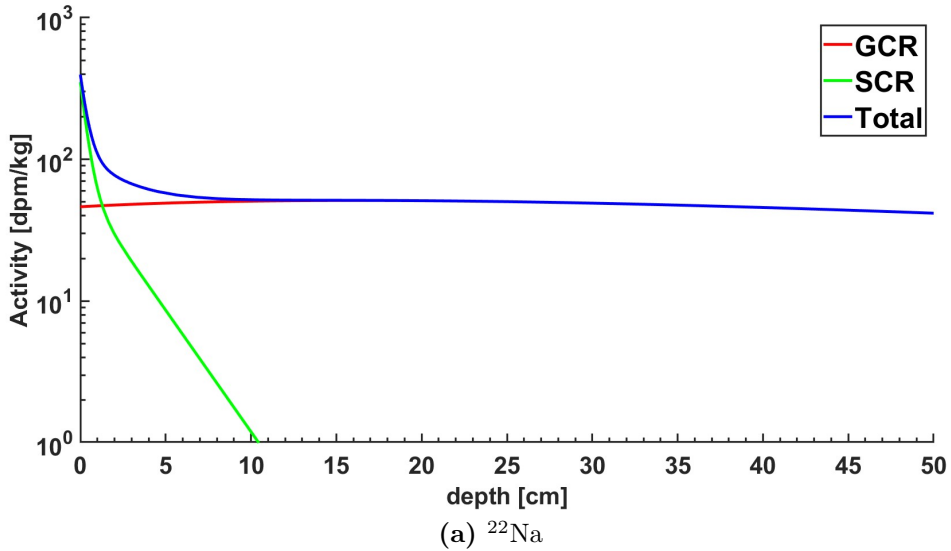


Figure 4.4: Total radioactivity up to 50 cm of depth.

4.4 GCR production - Geant4 model

Geant4 (GEometry ANd Tracking) is a Monte Carlo toolkit developed by the Geant4 Collaboration for the simulation of the interaction of particles passing through matter [1][2][3]. Geant4-based codes are primarily developed for high-energy experiments, such as BES III, ATLAS, LHC, and many others. However, the toolkit is well suited for other areas, such as space physics and medical physics. Thanks to its set of models, it covers all the physical processes fundamental for nuclear interactions, ranging from a few meV for neutrons up to TeV for all particles. The user finds great flexibility in correctly defining geometry, particle sources, and physics involved to simulate the phenomena of interest.

Geant4 has been recently employed in the cosmogenic radionuclides production field [32][25], demonstrating its deep versatility.

For this thesis, a model completely based on Geant4 for evaluating the nuclides activity trend in asteroids has been developed, validated, and then applied to Bennu.

4.4.1 The code

Geant4 automatically keeps track of every particle created during the simulation: for our purpose, the program fills histograms with the number of generated nuclides as a function of their radial position in the asteroid. See Figure 4.5 as an example. Note that the errors are calculated as the square root of the counts.

The code has been developed with the 10.7.03 version of the software and is based on the built-in hadronic example *Hadro06*, which has been modified to meet the physical situation we are interested in, as suggested by Peplowski et al. (2019) [32]. In order to easily access the different physics lists, the *G4PhysicsListFactory* class was implemented in the main script instead of the more common *PhysicsList* header, in which the user declares the physics to be used in the simulation. More details will be given later on the physics list selection. In order to represent the CR isotropic flux, the *G4ParticleGun* class, which allows for generating particles from point sources, was replaced with the *G4GeneralParticleSource*, which provides different source surface shapes and arbitrary energy and angular spectra for the particles.

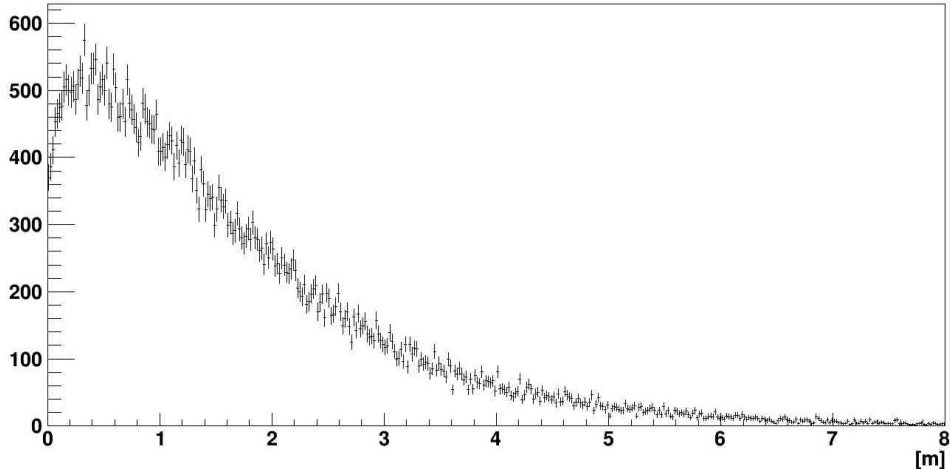


Figure 4.5: ^{26}Al radionuclides number depth distribution in Bennu. A total number of $5.8 \cdot 10^4$ nuclides were created in the asteroid by $4.4 \cdot 10^5$ incident protons, providing approximately one ^{26}Al isotope for every eight incident particles.

4.4.2 Particle generation

The target body is modeled as a homogeneous sphere, which is hit by GCR particles originating from a spherical surface. In order to implement the isotropic flux on the asteroid, the angular distribution of particle directions from the source surface follows a cosine law [33]:

$$J(\theta) = J_0 \cdot \cos(\theta) \quad (4.5)$$

where θ is the angle between the radial direction and the actual direction of the emitted particle. By implementing an isotropic angular distribution from the source surface, the resulting flux in the asteroid body is not isotropic. The situation is described in Figure 4.6. The cosine law distribution implies that the maximum emission probability is in the radial direction. This agrees with the real situation, in which CRs can be seen as emitted from a spherical surface of infinite radius, whereby the angle between the radial and the particle direction is always zero.

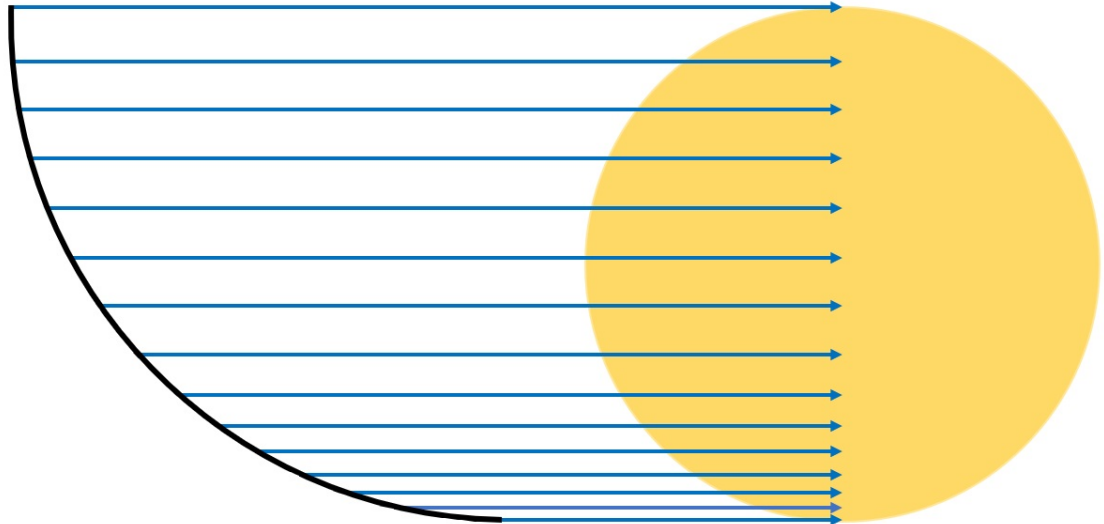


Figure 4.6: Isotropic irradiation from the source surface. Since the probability of emission is homogenous, the effect consists of denser field lines as the direction of emission approaches the tangent of the sphere. Image adapted from Santin (2007) [37].

As introduced before, both protons and α -particles were considered thanks to the parametrizations 3.2 and 3.5 for protons and 3.7 for alphas. These spectra are translated into binned energy histograms in order to be used by the code. As in the Geant4 built-in example *radioprotection*, we created a histogram with about 850 points for every modulation parameter for both protons and alpha particles. Each bar is calculated as the integral mean of the flux parametrization over the considered energy range, whose width varies according to the flux itself. The energy intervals increase their width along with the particle energies.

The secondary flux is automatically implemented in the code since Geant4 keeps track of every particle and nucleus created during the simulation. Therefore, the secondary neutron flux depends on both protons and α -particles.

As shown in Figure 4.5, the program creates histograms of radionuclides number as a function of their depth in the target body and fills them during the simulations. By simulating a certain amount of flux time, which is related to the number of protons/alphas, the number of radionuclides generated represents the number of decays in the same time-lapse thanks to the secular equilibrium hypothesis. Therefore the activity is directly determined. As in Peracchi et al. (2019) [33], once the statistics of the process are respected in the simulation, such as there are enough simulated particles that the number of radionuclides produced is directly proportional to the number of particles generated, the radioactivity obtained in the simulation timeframe can be converted into the desired activity (typically decays per minute) via direct proportionality:

$$A_{theo} = A_{sim} \frac{\Delta T_{theo}}{\Delta T_{sim}} \quad (4.6)$$

where ΔT_{theo} and ΔT_{sim} are linked to the number of generated particles.

The ΔT_{sim} -related number of particles can be determined by integrating the flux with the cosine law over the energies, half the solid angle, such as the emission angle, and the source surface S with radius R_{source} :

$$N = \int_S dS \int_0^{2\pi} d\phi \int_0^\infty \int_0^{\frac{\pi}{2}} J(\theta) \sin \theta \, d\theta \, dE = \int_0^\infty J_0 \, dE \int_S dS \int_0^{2\pi} d\phi \int_0^{\frac{\pi}{2}} \cos \theta \sin \theta \, d\theta \, d\phi \quad (4.7)$$

Operationally, it is unnecessary to simulate particles that do not hit the asteroid, so it is useful to limit the emission direction so that, at most, the particles are tangent to the target (equation 4.8). This is done by implementing a maximum value of θ . Each integral in the formula is independent of the others and can be resolved:

$$\begin{aligned}
 N &= \int_0^\infty J_0 \, dE \int_S dS \int_0^{2\pi} d\phi \int_0^{\theta_{max}} \cos \theta \sin \theta \, d\theta = \\
 &= 4\pi R_{source}^2 2\pi \frac{\sin^2 \theta_{max}}{2} \int_0^\infty J_0 \, dE = \\
 &= 4\pi^2 R_{source}^2 \sin^2 \theta_{max} \int_0^\infty J_0 \, dE
 \end{aligned} \tag{4.8}$$

In Figure 4.7, the simple trigonometric relationship between the radius of the source surface, the meteorite radius, and the maximum angle of emission can be seen. The relationship is described by the following equation:

$$R_{asteroid} = R_{source} \sin \theta_{max} \tag{4.9}$$

Therefore, the number of particles to be generated to simulate a certain amount of flux is finally given by equation 4.10, where the "amount of flux" depends on the integration over the energies of the flux parametrization:

$$N = 4\pi^2 R_{asteroid}^2 \int_0^\infty J_0 \, dE \tag{4.10}$$

Since the flux influences every isotope at least in the three past half-lives, attention must be paid to how the secular equilibrium is implemented and with what flux intensity. A method of the determination of the correct modulation parameter to be applied is now described.

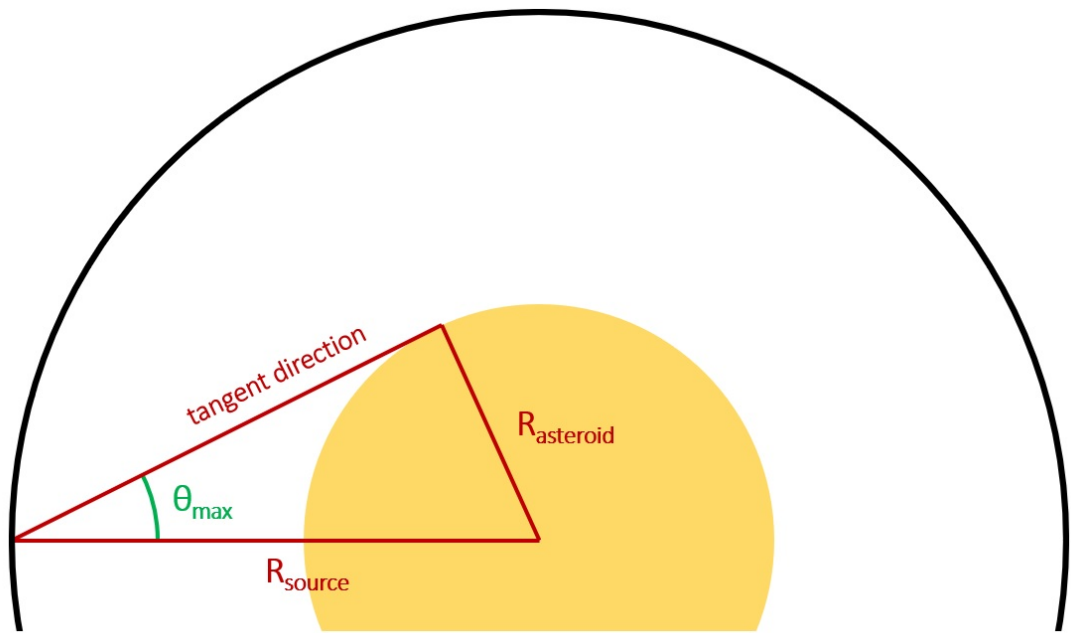


Figure 4.7: Relationship between source surface and astroid radii and θ_{max} . Note that this logic is possible due to the fact that the asteroid and the source surface are concentric.

4.4.3 Secular equilibrium-related modulation parameter

As explained in subsection 3.2.4, the GCR flux intensity depends on the modulation parameter, which varies according to solar activities oscillations. By assuming the secular equilibrium, such as the balance between production and destruction of the radioisotopes, we can easily calculate a nuclide activity by evaluating the production rate related to a certain GCR flux intensity. However, as explained in section 3.3, a radionuclide is useful to study the GCR flux in its past three half-lives, which means that one cannot simply simulate the instantaneous GCR flux at a given time to correctly estimate its radioactivity. Some sort of mean value of the past GCR flux must be taken into account.

Here, a method to obtain a suitable modulation parameter for each radionuclide based on its half-life is presented. The approach is similar to the one used for the $^{22}\text{Na}/^{26}\text{Al}$ ratio in subsection 3.3.2. By exploiting Usoskin's series up to October 2020, such as the month of sampling, the weighted average of the modulation

parameter, with the radioactive decay exponential law as weight, is calculated as:

$$\bar{M}[n] = \frac{\sum_{i=1}^n M[i] \cdot e^{-\lambda(t_n - t_i)}}{\sum_{i=0}^n e^{-\lambda(t_n - t_i)}} \quad (4.11)$$

where n is the index representing October 2020 in this case. The modulation parameter in October 2020 weights 1, while past the modulation parameter weights less and less going back in time, with a null weight at the minus infinity limit.

Thanks to equation 4.11, we determined the modulation parameters needed for simulating ^{44}Ti , ^{60}Co , ^{22}Na , ^{54}Mn , and ^{57}Co (Table 4.2). The series is too short for ^{26}Al , for which we used the mean value of 660 MeV, estimated by Leya et al. (2021) [25]. Note that the series covers less than two ^{44}Ti half-lives; therefore, the actual value with the hypothetical complete modulation parameter series could be different.

^{26}Al	^{44}Ti	^{60}Co	^{22}Na	^{54}Mn	^{57}Co
660	503	373	309	229	223

Table 4.2: Average modulation parameters for protons in MeV, calculated with expression 4.11, with exception for ^{26}Al .

As seen in Figure 3.4, the GCR spectrum significantly varies along with the modulation parameter. Thus, the number of protons and α -particles to be simulated for each modulation parameter value must be calculated. In Table 4.3, the number of particles per second hitting Bennu can be seen. Due to the limits of our computational resources, only a fraction of the particles were generated in the simulations. In particular, we found that numbers equal to $10^{-4} N_p$ and $10^{-3} N_\alpha$ for protons and α -particles, respectively, are sufficient to satisfy the statistics of the simulation.

M	$\int_0^{\infty} J_{0,p} dE$	N_p	$\int_0^{\infty} J_{0,\alpha} dE$	N_{α}
660	$1.9 \cdot 10^3$	$4.4 \cdot 10^9$	$2.3 \cdot 10^2$	$5.2 \cdot 10^8$
503	$2.6 \cdot 10^3$	$5.9 \cdot 10^9$	$2.8 \cdot 10^2$	$6.4 \cdot 10^8$
373	$3.3 \cdot 10^3$	$7.7 \cdot 10^9$	$3.4 \cdot 10^2$	$7.8 \cdot 10^8$
309	$3.9 \cdot 10^3$	$8.9 \cdot 10^9$	$3.8 \cdot 10^2$	$8.7 \cdot 10^8$
229	$4.8 \cdot 10^3$	$10.0 \cdot 10^9$	$4.4 \cdot 10^2$	$10.0 \cdot 10^8$
223	$4.9 \cdot 10^3$	$11.1 \cdot 10^9$	$4.4 \cdot 10^2$	$10.1 \cdot 10^8$

Table 4.3: Protons and α -particles per second hitting Bennu. The integral of the flux parametrization is in particles/(m² sr s) units, while N_p and N_{α} are in particles/s units. M is in MeV units as before.

4.4.4 Physics list selection

The selection of a physics list is crucial for a Geant4 simulation. Each physics list represents a different numerical model of possible particle interactions. In the case of the radionuclides production topic, the physics involved lies in the transport of the primary particles through matter, the generation of secondary particles, and the primary and secondary particle-induced intranuclear and internuclear cascades that lead to the production of nuclides.

In light of the purpose of this thesis, the interest is in the differences between the hadronic interaction models in each physics list (Figure 4.8). Peplowski et al. (2019) [32] identified five potential physics lists suitable for the cosmogenic radionuclides production problem: QGSP_BIC_HP, QGSP_BERT_HP, FTFP_INCLXX_HP, Shielding, and QBBC, where the _HP suffix implies the use of the NeutronHP class, which provided high precision neutron cross-section libraries.

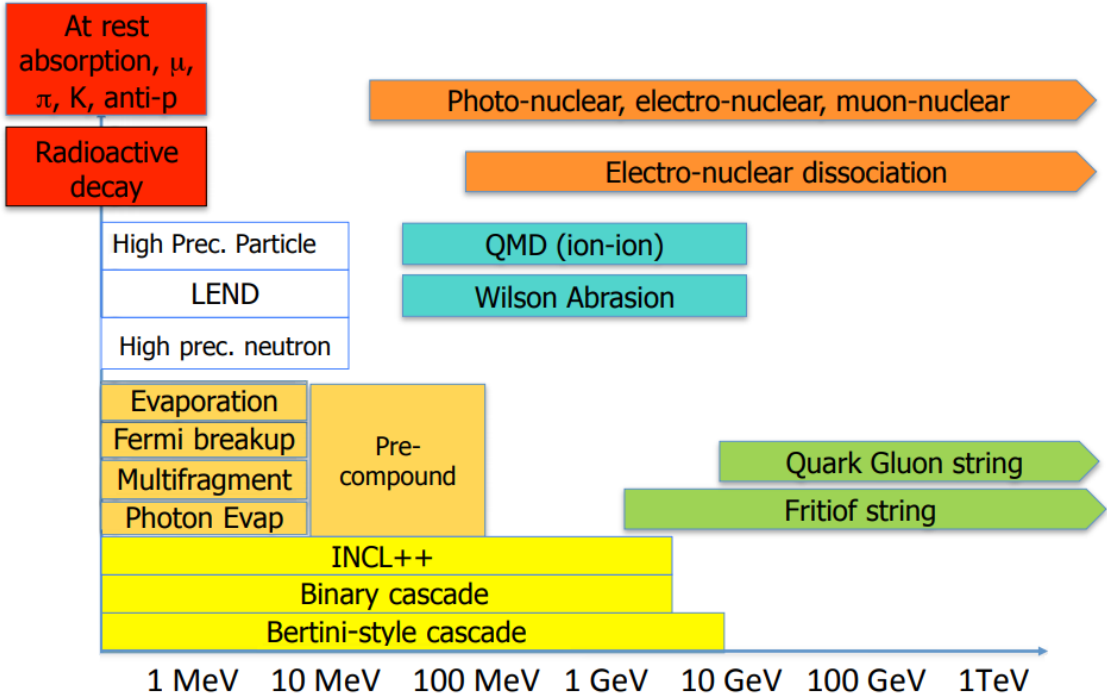


Figure 4.8: Geant4 hadronic models.

Figure adapted from <https://wuhongyi.cn/Geant4Note/PhysicsProcesses>

- The *Precompound* model performs the de-excitation of the nuclei that remains after a high-energy collision [34].
- In the *Liege Intranuclear Cascade (INCL)* model, the high-energy incident particles initiate an avalanche of binary collisions with the target nucleus. The cascade stops when the remnant nucleus shows signs of thermalization [19].
- The *Binary Ion Cascade (BIC)* model is a hybrid model between a classical intra-nuclear cascade and a quantum molecular dynamics (QMD) model. The nuclei are modeled by individual nucleons bound in the nuclear potential. Binary collisions are simulated according to measured, parametrized, or calculated cross-sections [16].
- The *Bertini (BERT)* cascade model is a classical model which solves, on average, the Boltzmann equation for the transport of a particle through a gas of nucleons [50].

- The *Quark Gluon String (QGS)* is the basic physics list applying the quark-gluon string model for high-energy interactions of protons, neutrons, pions, Kaons, and nuclei [49]
- The *Fior tof (FTF)* model assumes that, in the course of a hadron-nucleus interaction, the string originating from the projectile can interact with various intra-nuclear nucleons and evolve into highly excited states [44].

In Geant4, both QGS and FTF models are associated with the Precompound model for the de-excitation of the nuclei, therefore being named QGSP and FTFP. The above-mentioned physics lists use a combination of the hadronic models based on the particle's energy, as can be deduced by their name, except Shielding and QBBC.

The Geant4 official website recommends the former for shielding applications and underground physics. It is based on FTFP_BERT_HP and includes cross-sections derived from the Japanese Evaluated Nuclear Data Library [38].

QBBC utilizes a combination of QGSC and FTFC (QGS and FTF with CHIPS model for the de-excitation, such as the CHiral Invariant Phase Space model) for high energies, while a combination of BERT and BIC for the low energies, and a neutron cross-section model instead of the cross-section libraries to improve computational time.

In order to select a proper physics list, we reproduced the results of the experiment from Peplowski et al. (2019) [32], and the radioactivity in the Knyahinya meteorite [18], as done by Leya et al. (2021) [25]. See the references for the meteorite compositions.

Peplowski's experiment consisted in the irradiation of two slabs of different materials, an iron meteorite and a bronzite pyroxenite, with a beam of 1-GeV protons, and the measurement of the radioisotopes produced. We simulated the same experimental set-up, obtained the expected radioactivity of different isotopes according to the five physics lists, and then compared them with the actual experimental results via gaussian tests (Figures 4.9 and 4.10). Great variability in the outcomes can be seen: ^{52}Mn in the iron meteorite is not correctly described by any of the models, while it is the opposite for ^{54}Mn for both compositions. Note that

QGSP_BERT_HP results are not visible because they are superimposed on the Shielding results.

For the purpose of simulating the radionuclides activity in Bennu (Table 3.1), the focus is on ^{54}Mn , ^{22}Na , and ^{57}Co . As already said, ^{54}Mn is correctly described by all the physics lists. The same happens in the bronzite pyroxenite for ^{22}Na , with the Shielding list giving the best accuracy. ^{57}Co seems to be correctly produced only by the QBBC list.

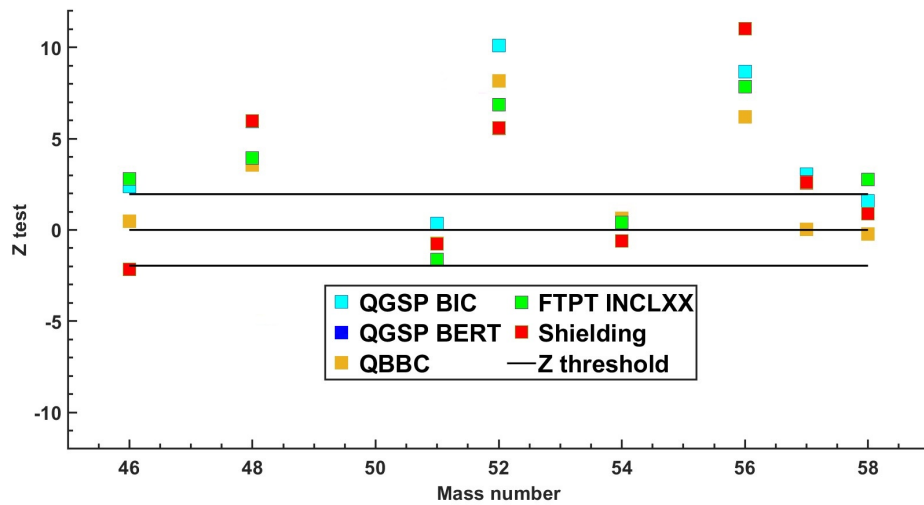


Figure 4.9: Z-tests between the expected radioactivities from the Geant4 simulation and the measured radioactivities in the experiment. On the x-axis there are the mass numbers of the isotopes: ^{46}Sc , ^{48}V , ^{51}Cr , ^{52}Mn , ^{54}Mn , ^{56}Co , ^{57}Co , and ^{58}Co .

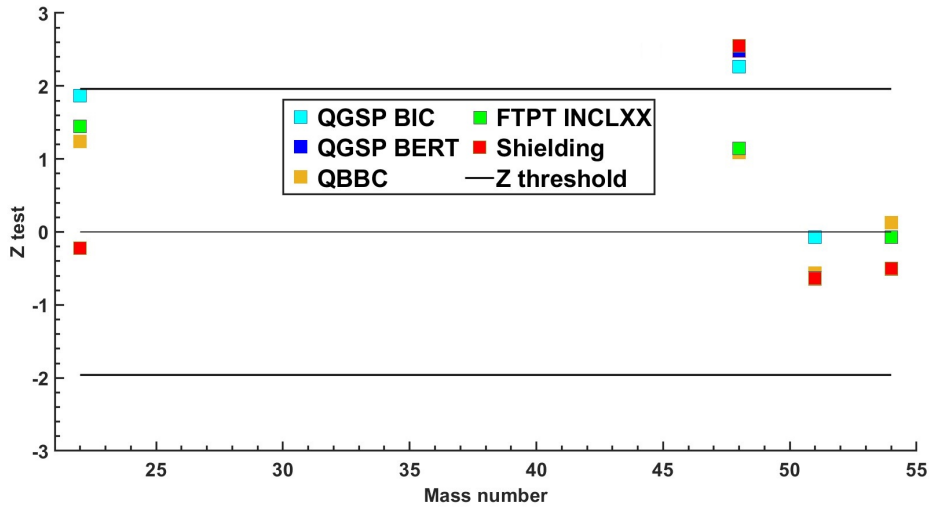
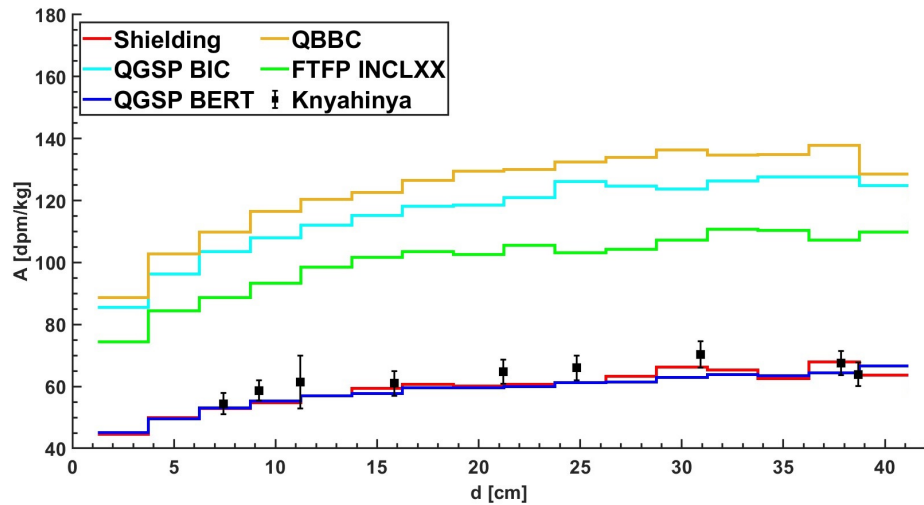


Figure 4.10: Z-tests between the expected radioactivities from the Geant4 simulation and the measured radioactivities in the experiment. On the x-axis there are the mass numbers of the isotopes: ^{22}Na , ^{48}V , ^{51}Cr , ^{54}Mn .

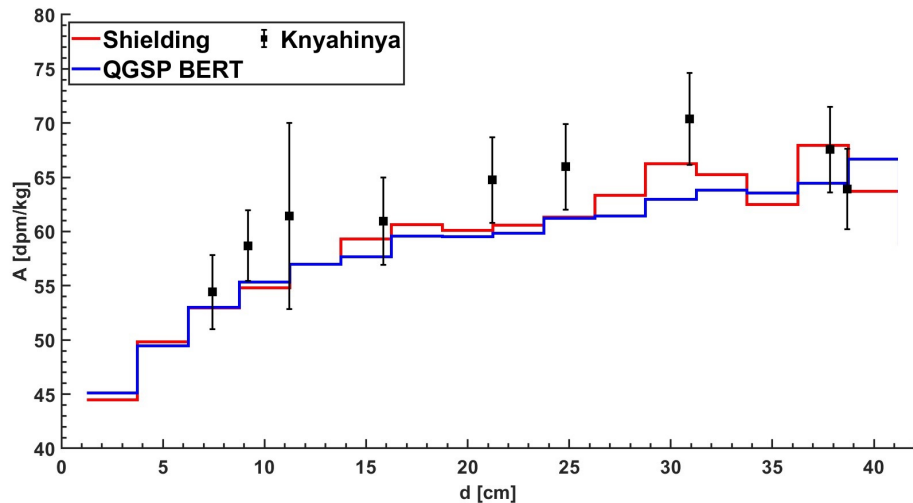
We also reproduced the ^{26}Al activity trend in the Knyahinya L chondrite (Figure 4.11). Knyahinya fell on June 9, 1866, in Nagybereszna, Ukraine, with a shower of more than 1000 fragments and the main mass of 300 kg breaking into three pieces. Graf et al. (1990) [18] produced a nearly planar cross-section of the main mass, passing close to its center, from which the analyzed samples were taken. According to the paper, the coordinates have considerable errors, ranging from 2 to 5 cm depending on the depth of the sample. See the reference for the experimental procedure and more details on the results.

A good description of ^{26}Al by the code is fundamental because it is one of the most produced radionuclide in celestial bodies and gives information on the GCR flux on a long time scale. The presence of ^{26}Al determines whether the object has extraterrestrial or terrestrial origins since it cannot be naturally produced on Earth.

The QBBC list, which was the best candidate until now, results in being the worst model for ^{26}Al . QGSP_BERT_HP and Shielding have the best accuracy: their results mostly fall within the error bars of the experimental data.



(a) Reproduction of Knyahinya experimental activity trend.



(b) Reproduction of Knyahinya experimental activity trend with Shielding and QGSP_BERT_HP.

Figure 4.11: Test of the physics lits with the data from the Knyahinya chondrite. In this case, the *stairs plot* was used because the errors related to the counts in the histograms were neglectable.

Due to the importance of ^{26}Al , the QBBC list cannot be considered suitable anymore. For computational time considerations, the Shielding physics list has been selected over QGSP_BERT_HP as the best model to describe the radionuclides production we are interested in. From now on, all the results must be intended to be obtained with this physics list.

In the next chapter, the two models for GCR production will be compared. The Geant4 model will be validated by reproducing the $^{22}\text{Na}/^{26}\text{Al}$ ratio, and an estimation of the radioactivity of the surface material sample will be provided.

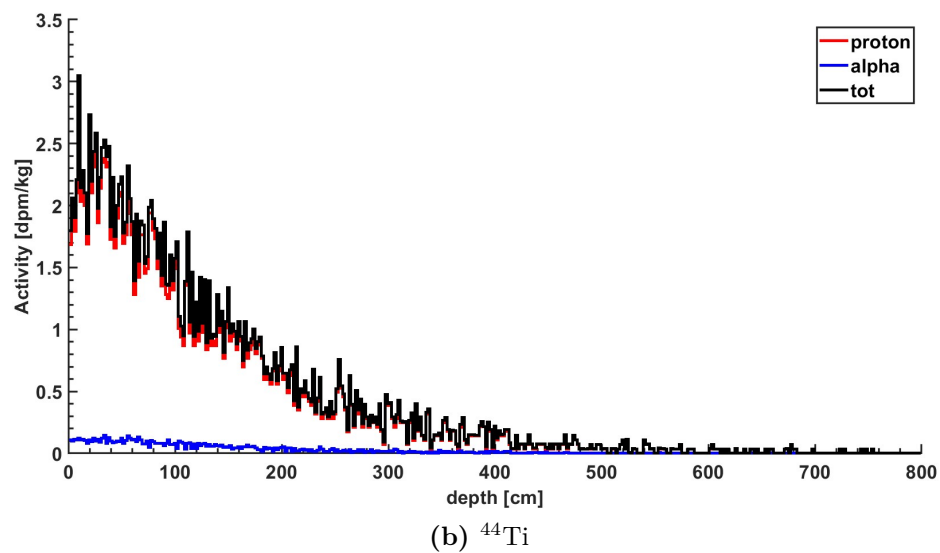
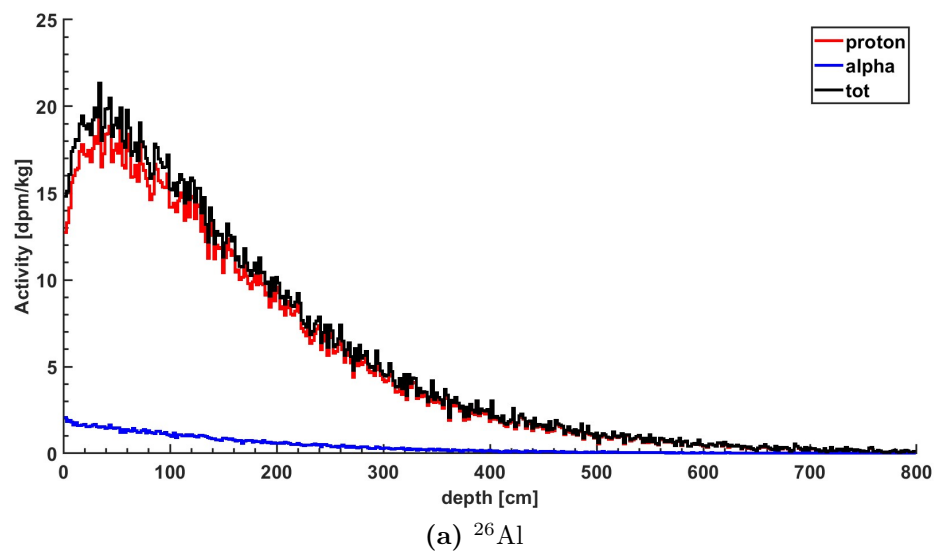
Chapter 5

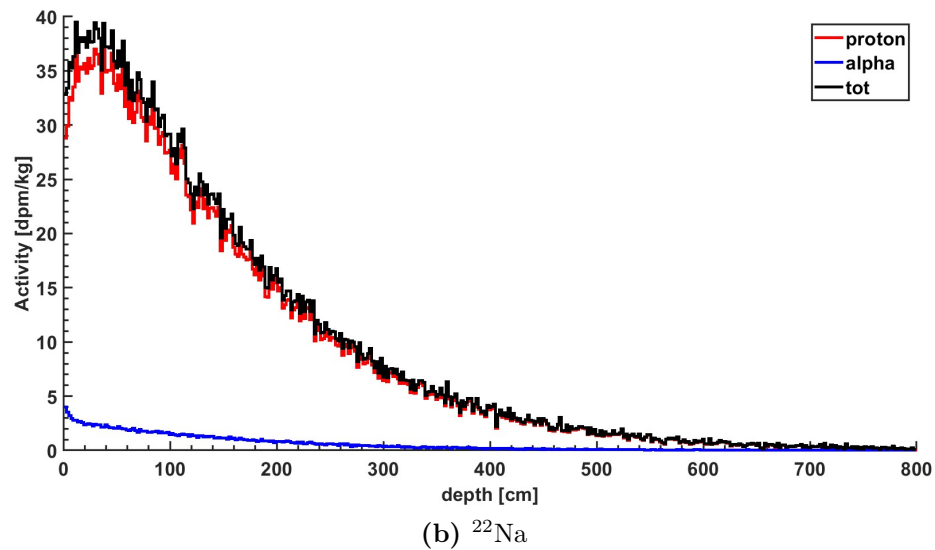
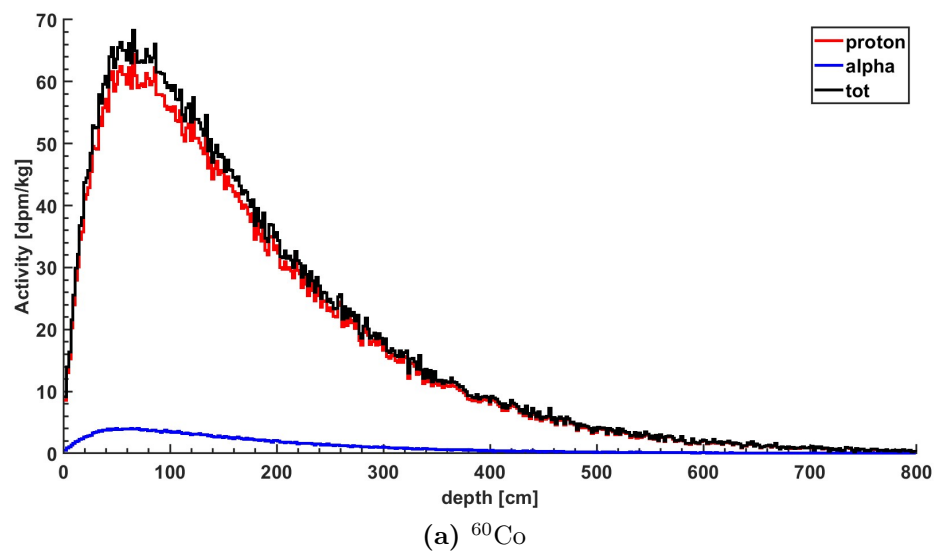
Results and comparisons of the models

5.1 Results of the Geant4 simulation

In light of the characteristics described in section 4.4, the simulation was run for the six radionuclides of interest. In the following figures (Figure 5.1), the proton-induced, alpha-induced, and total GCR-related activities of the six radionuclides can be seen. These simulations were executed by assuming Bennu’s average bulk density (Table 1.3) as the constant density of the modeled asteroid. After several tests, we noted that the production is negligible over 8 meters of depth for every radionuclide.

^{44}Ti is poorly produced, and the resulting activity shows profound randomness in its trend. About 1 ^{44}Ti nucleus is created every 115 incident protons with a 503 MeV modulation parameter, while 13 ^{26}Al nuclei are produced by 115 protons with the same flux intensity. In order to satisfy the statistics of ^{44}Ti , at least a number of protons equal to $10^{-3} N_p$ (referred to Table 4.3) must be simulated.





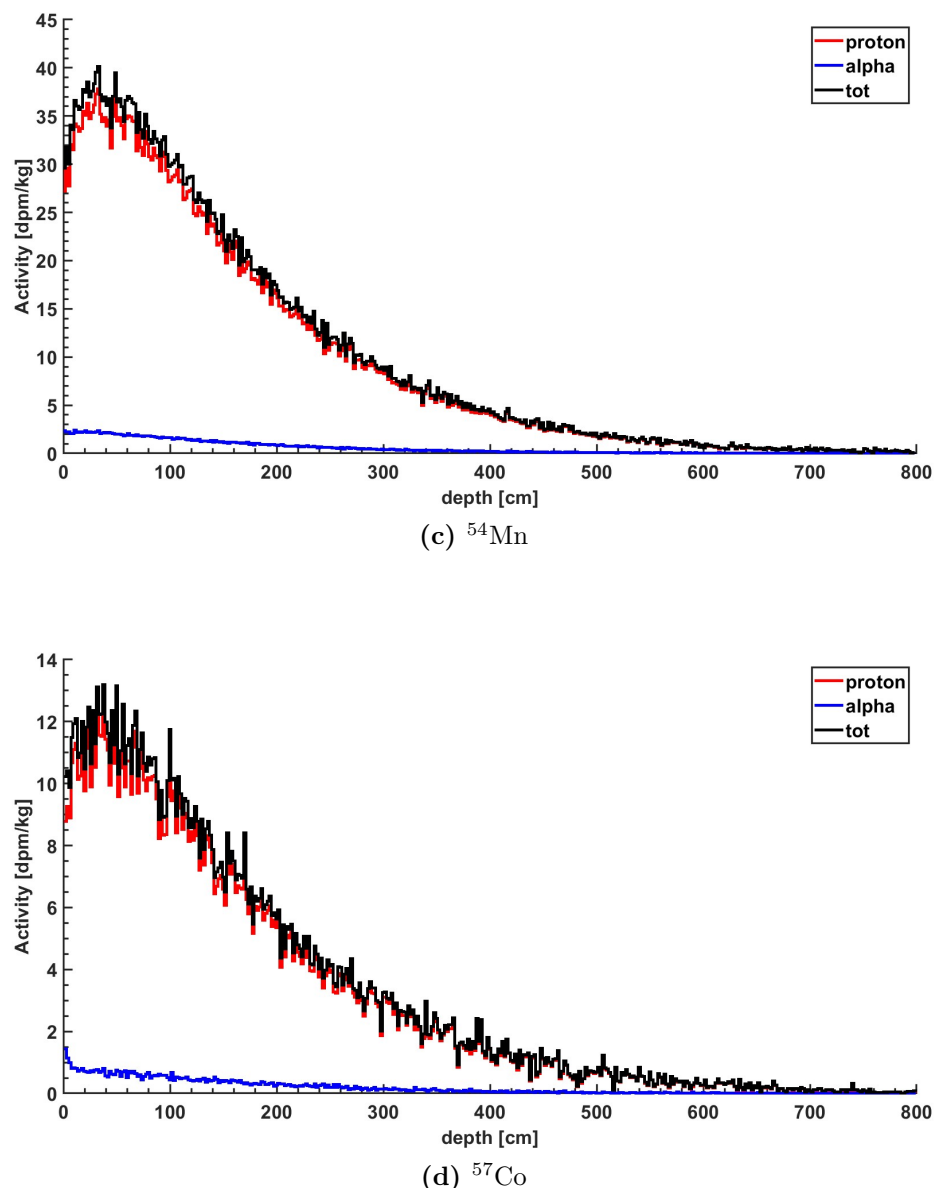
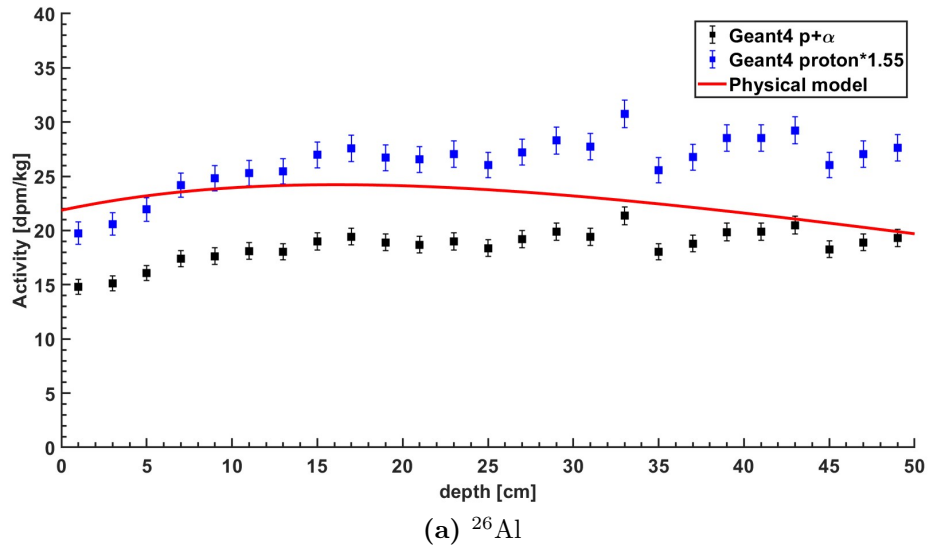


Figure 5.1: Radioactivity in Bennu.

5.2 Comparison of the models

A further validation of the Geant4 model comes from comparing the results of the two approaches for GCR-induced radioactivity. In Figure 5.2, the results from the physical model, the Geant4 model with protons and alphas, and the Geant4 model with protons with the application of equation 4.4 (which is the same applied to the physical model) are shown. We can see that the Geant4 model with protons and α -particles provides a lower activity than the physical model, while the Geant4 model with equation 4.4 provides higher values. Moreover, the peaks of the Geant4 results appear to be at higher depths. This can be due to the fact that in the Geant4 simulation we implemented Bennu's estimated average radius, while for the physical model we assumed an infinite radius.

A comparison between how the α -particles are considered in both models can be made. By plotting the ratio between α -induced and proton-induced activities (Figure 5.3), we can see that directly simulating α -particles leads to an activity consistently lower than scaling the proton-induced activity by the 0.55 factor. This aspect is emphasized for ^{22}Na .



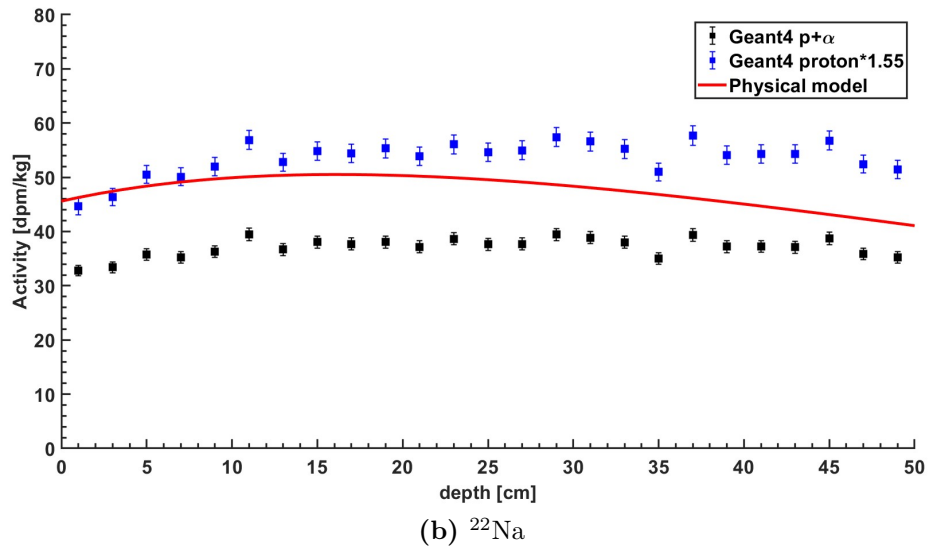


Figure 5.2: Comparison between the activities of ^{26}Al and ^{22}Na calculated with the Geant4 and Physical models.

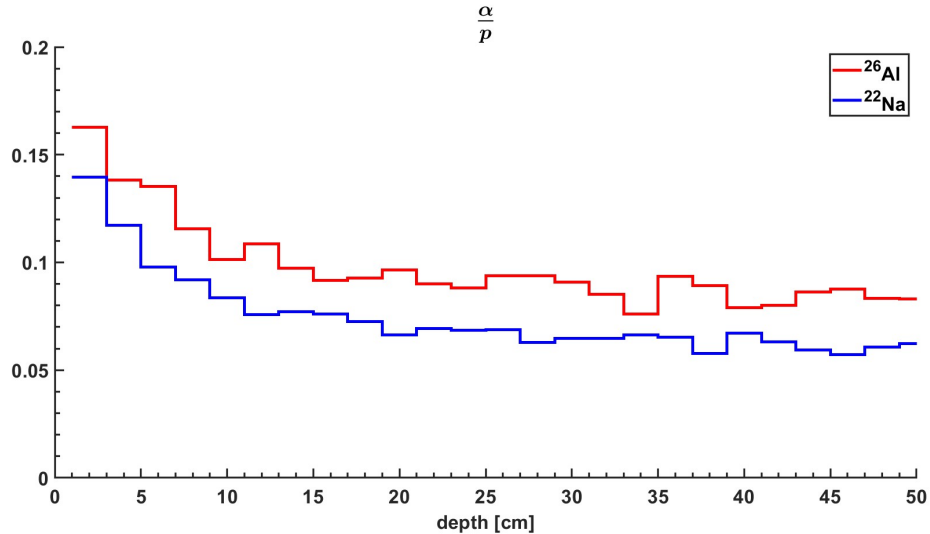


Figure 5.3: Comparison between ^{26}Al and ^{22}Na α -induced and proton-induced activities in the Geant4 simulation. The ratio starts at a value of 0.16 for ^{26}Al and then seems to decrease to a constant asymptote. The same happens for ^{22}Na with lower values.

5.3 Reproducion of $^{22}\text{Na}/^{26}\text{Al}$ trend

As explained in subsection 3.3.2, the ratio between ^{22}Na and ^{26}Al gives information about the solar activity level in the decadal cycle time-span and we used this ratio to estimate ^{22}Na radioactivity in Bennu (section 4.2) for the physical model calculations. Since the ratio does not depend on asteroid/meteorite size and depth, it is useful to determine a function linking the ratio to the modulation parameters at fixed asteroid/meteorite composition. With the new Geant4 model, we simulated the production of ^{26}Al with 660 MeV rigidity and ^{22}Na with rigidities spanning from 100 MeV to 1000 MeV in three spherical bodies with different compositions:

- CM chondrite with 241 m radius (Bennu)
- H chondrite with 30 cm radius
- L chondrite with 45 cm radius

For more details about meteorite clarification and chondrites, see Appendix A. By dividing the ^{22}Na activities with ^{26}Al average activity, we obtained three functions for the ratio (Figure 5.4).

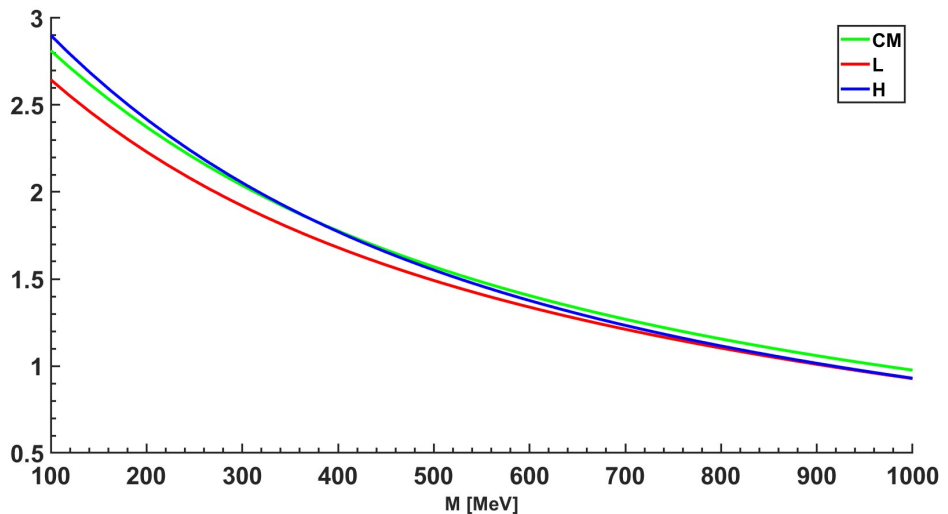
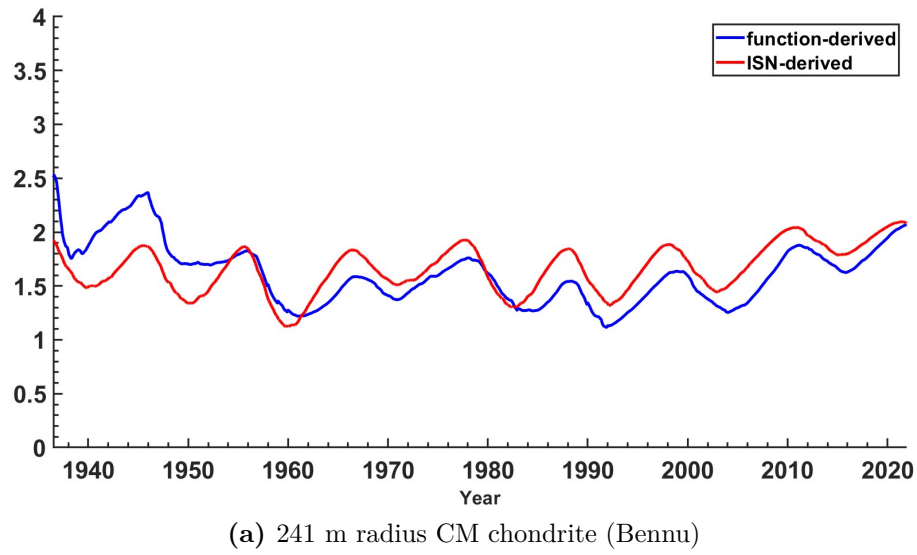


Figure 5.4: $^{22}\text{Na}/^{26}\text{Al}$ activity ratio for H, L, and CM chondrite compositions.

It is possible to compare the radioactivity ratio trends of the three compositions, given by the calculation with the ISN series (method in subsection 3.3.2), and the trends obtained by the ratio functions in Figure 5.4. By applying these functions to Usoskin's series through equation 4.11 for the secular equilibrium hypothesis, we obtain the results in Figure 5.5. Note that the average ratios for L and H chondrites are 1.35 and 1.5, respectively, calculated again with Reedy and Arnold's (1972) [35] semi-empirical model.



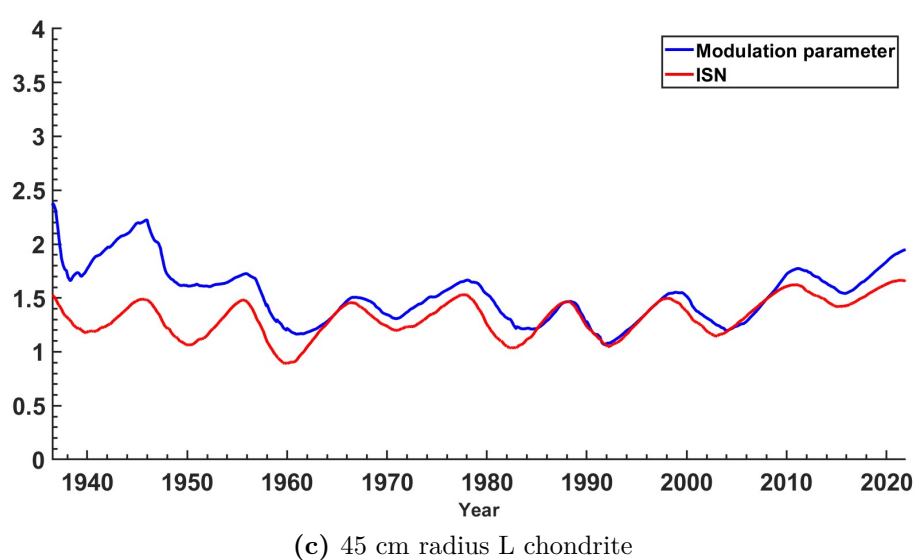
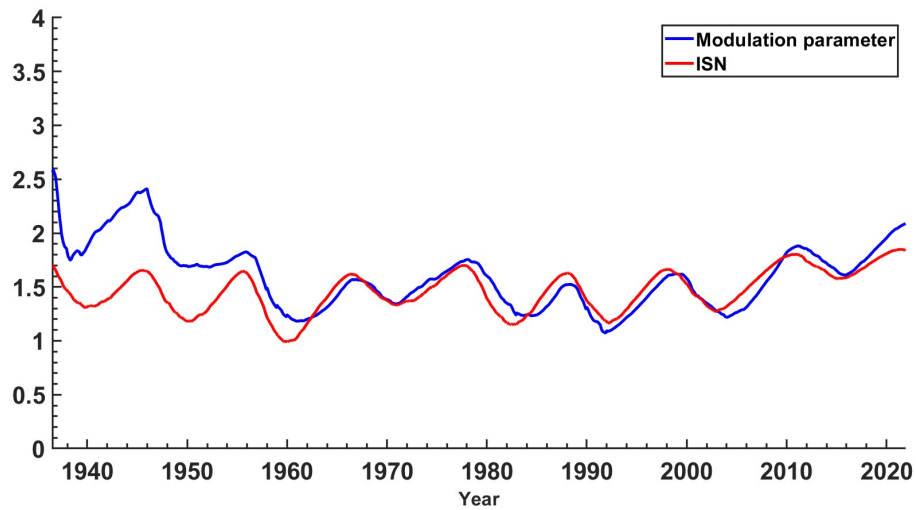


Figure 5.5: Reproduction of $^{22}\text{Na}/^{26}\text{Al}$ ratio.

It must be noted that the modulation parameter series begins in 1936, and since ^{22}Na half-life is 2.6 years, at least the first ten years of the prediction should not be taken into account, because the mean modulation parameter is not calculated with enough values.

There is a good agreement between the trends for H and L compositions between 1964 and 2008. The CM composition shows an agreement between the two trends between 1956 and 1982, after which the ratio calculated with the Geant4 model provides systematically lower values. After 2020, the function-derived curve seems to rise again to match the ISN-derived curved.

The expected ratios in October 2020 are in agreement between the two models, giving 2.1 and 2.0 for the ISN and the function method, respectively.

5.4 Sample radioactivity and ^{26}Al saturation

As anticipated in section 4.3, there is a one-to-one correspondence between the mean activity in the sample and the sample depth. This allows for determining the sample depth after the radioactivity measurements on the sample. Note that by applying the integral mean to the total activity trend to determine the radioactivity of the sample, we automatically hypothesize that the surface material is homogenous and that a uniform sampling in depth took place.

The average activity of ^{26}Al and ^{22}Na in Bennu up to 50 cm of depth is shown in Figure 5.6. Note that this trend is obtained by combining physical and semi-empirical models, thanks to which we could estimate the total (GCR + SCR) activity.

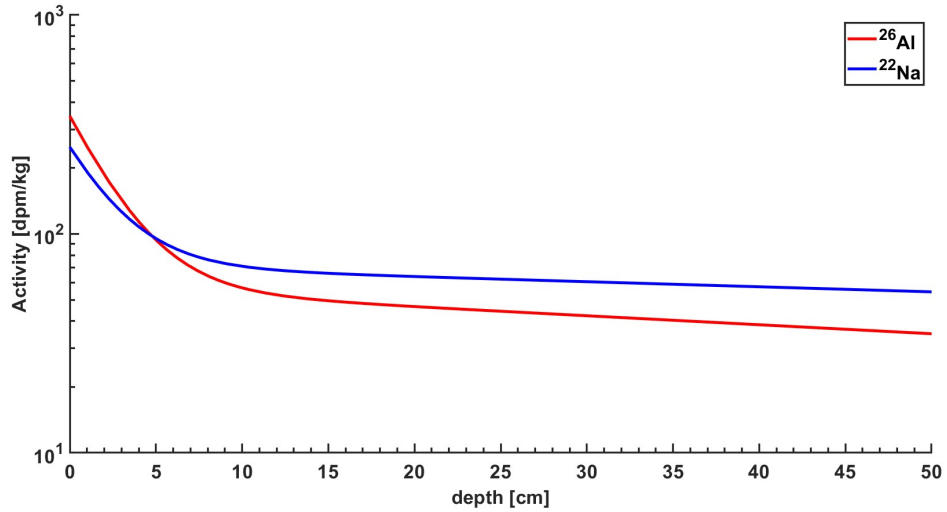


Figure 5.6: ^{26}Al and ^{22}Na mean activity as a function of depth.

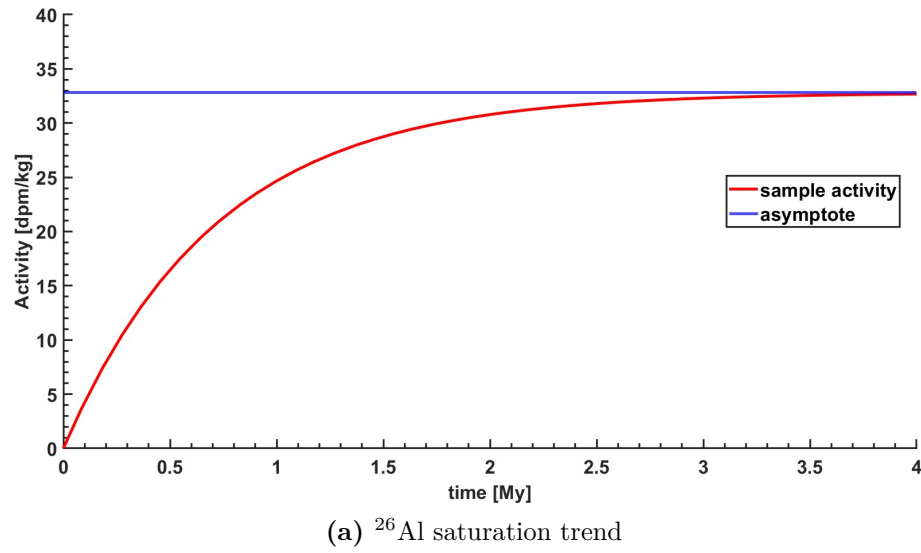
According to Lauretta et al. (2022) [22], the maximum depth reached by the TAGSAM is 48.8 cm. Based on his estimation, we calculated the expected radioactivity of the sample with the hypotheses explained above. With the development of the calculations so far, we are able to provide the estimation for ^{26}Al and ^{22}Na because we have both SCR and GCR production for them, and ^{60}Co because it is formed by neutron capture and neutrons are produced only by the GCR primary flux, which we have calculated through the Geant4 simulation. In the next table (Table 5.1), the results are shown.

^{26}Al	^{22}Na	^{60}Co
33 dpm kg $^{-1}$	54 dpm kg $^{-1}$	45 dpm kg $^{-1}$

Table 5.1: Expected radionuclides in Bennu's surface sample.

The expected activity of ^{26}Al also represents the number of nuclides produced in one minute per kilogram by the CRs with the hypothesis of secular equilibrium. Thanks to this value, we can draw the ^{26}Al saturation trend as a function of time, as introduced in subsection 3.3.1. After the γ -measurements at Monte dei Cappuccini

Laboratory, this graph will be useful to determine the exposure age of the asteroid. Due to its long half-life, the experimental ^{26}Al radioactivity will tell us how long the asteroid has been hit by CRs, confirming the production saturation hypothesis or maybe unraveling a much younger age of the celestial body. Since ^{22}Na will be saturated by the production with a typical modulation parameter given by Table 4.2, a similar saturation trend can be drawn for the $^{22}\text{Na}/^{26}\text{Al}$ ratio. Both results can be seen in Figure 5.7.



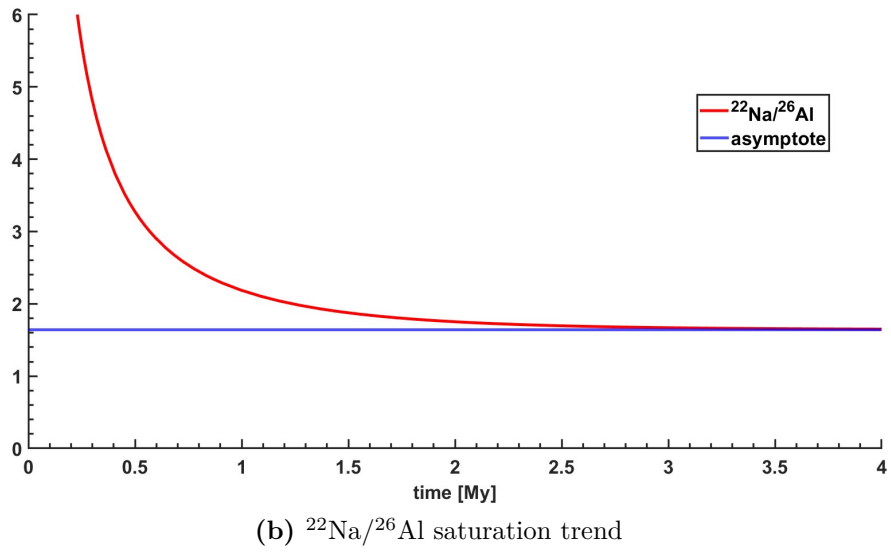


Figure 5.7: Saturation trends for ^{26}Al and $^{22}\text{Na}/^{26}\text{Al}$. Note that the asymptote for the ratio is calculated with the expected total activity of the sample, which includes the SCR production and therefore is different from the ratio calculated for just the GCR production.

Chapter 6

Conclusions

6.1 The Geant4 model

The new Geant4 model is in partial agreement with the experiment in Peplowski et al. (2019) [32] and correctly describes the ^{26}Al activity trend in the Knyahinya chondrite. With the continuous development of the toolkit, the model could lead to a better description of more radionuclides. It could represent a simple and easy-to-use method for cosmogenic radioactivity estimations.

The two methods of calculating the $^{22}\text{Na}/^{26}\text{Al}$ ratio are in general agreement in particular time intervals of the past century for the H, L, and CM compositions. Moreover, the ^{22}Na activities calculated with the physical model and Geant4 in Bennu show similar values. This suggests the correctness of the mean weighted with the exponential law to determine the modulation parameter representing the secular equilibrium.

Thanks to these properties, the Geant4 models appear to have two main applications:

- The estimation of the radioactivity in a celestial body once the GCR flux history is known (modulation parameter series), as we did in this work.
- The estimation of the GCR flux history once the experimental activity of the hypothetical sample is determined. A series of simulations for radionuclides with different half-lives can be carried out to find the correct modulation

parameter that leads to the experimental radioactivities. In this way, a series of average GCR flux over different periods is discovered, giving information about solar activity variations in the past.

6.2 Activity of the sample

Thanks to the semi-empirical model, the physical model, and the Geant4 model, we were able to estimate the average ^{26}Al , ^{22}Na , and ^{60}Co activities of the sample. Once the amount of material to be provided to the Monte dei Cappuccini Laboratory is declared, these estimations will be helpful in foreseeing the time of measurement needed for the GEM 150 to obtain a specific error.

The experimental ^{26}Al will provide information about the exposure age of the surface from which the material was sampled: a particular value of ^{26}Al activity, or $^{22}\text{Na}/^{26}\text{Al}$ ratio, corresponds to a unique exposure time through the saturation curves.

Chapter 7

Future plans

The measurement of the material will have a variable duration depending on the actual mass that will be provided. Radioisotopes with short half-lives will be useful to reveal the solar activity imprint during the return journey. ^{26}Al activity will be crucial for the determination of the exposure age of the asteroid.

If also ^{44}Ti will be revealed, a simulation with more particles can be run to estimate its activity correctly. Comparing the expected and experimental results can help understand the code's capability to describe the production phenom. Meanwhile, the program will be developed further, with various possible paths to follow, not necessarily mutually exclusive:

- Following Leya et al. (2021) [25], the program could be specialized just in the evaluation of the primary and secondary spectra. The activities would be calculated using the physical model formula with the most updated cross-sections.
- The target body could be generalized to any shape. This would imply the loss of the activity radial trend in favor of a 3-D plot of the specific activity of each body, providing a more detailed description of the radioactivity of a hypothetical sample, which depends on the sampling site.
- With the new versions of the Geant4 code, there could be better agreement by the Shielding physics list (or any other) with experimental data.

- The SCR particles can be implemented in the simulation with their energy spectra.

Appendix A

Classification of meteorites

The majority of meteoroids originate from collisions between larger objects, especially in the main asteroid belt. If a meteoroid transits through Earth's atmosphere, it undergoes the so-called ablation process, such as the removal of material from its surface due to friction and high frontal compression, and it is called a meteor. Meteorites consist of the remaining fragments of meteors that reach the ground on Earth.

Meteorites are named after their place of fall or find and classified according to their mineralogical, petrological, chemical, and isotopic properties. Meteorites with similar classifications may have a common origin and come from the same parent body. See Gattachecca et al. (2021) [17] for the latest *Meteorite Bulletin*, in which the official identification, naming, and classification of meteorites are made.

Meteorites are divided into three leading families: chondrites, such as meteorites that underwent little change since their parent bodies initially formed and characterized by near-spherical melted grains of silicates called chondrules; achondrites, such as meteorites with complex origin and lacking chondrules; primitive achondrites, with intermediate properties. These three clusters are further divided into classes and groups as shown in Figure A.1. However, it must be noted that new types of meteorites are frequently discovered. Therefore, this classification is constantly evolving. Moreover, there are meteorites that do not fit into any class.

Concerning their chemical composition, meteorites are often divided into three categories based on the dominant material they are composed of: stony meteorites,

mainly composed of silicate minerals; iron meteorites, primarily or entirely composed of metallic iron and nickel, and stony-iron class meteorites, consisting of an intermediate composition of the previous.

Chondrites represent about the 90% of recovered meteorites, and the majority of them belong to the ordinary class, which can be divided into three subclasses depending on the concentration of Fe and other metals: H chondrites, with a high level of Fe, L chondrites, with a low level of Fe, and LL chondrites with low levels of Fe and metals.

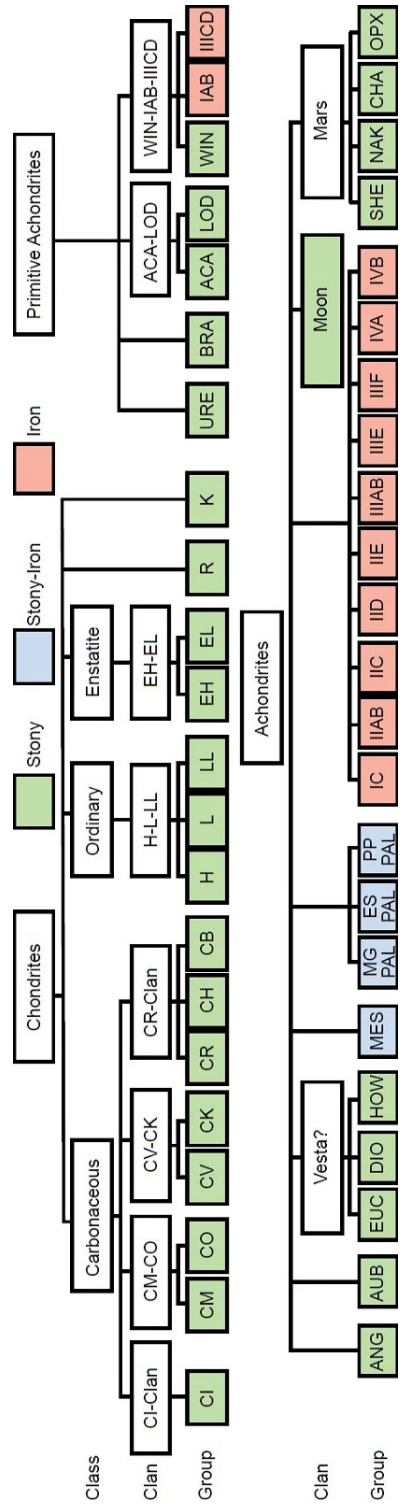


Figure A.1: Classification of meteorites from Snelling (2015), adapted from Weisberg, McCoy, and Krot (2006) [48].

List of Tables

1.1	Subclassification of NEAs, with a semi-major axis, Q aphelion distance, q perihelion distance, and H absolute magnitude.	8
1.2	Bennu’s expected composition as a CM chondrite [26].	10
1.3	Bennu’s orbital parameters and absolute magnitude, where i is the inclination of the orbit, T is the revolution period, e is the eccentricity, ρ is the average bulk density, and d is the average diameter.	12
3.1	Expected radionuclides in Bennu’s surface sample. The half-lives are updated to Kondev et al. (2021) [20].	36
4.1	Parameters of the production rate equation 4.3.	40
4.2	Average modulation parameters for protons in MeV, calculated with expression 4.11, with exception for ^{26}Al	51
4.3	Protons and α -particles per second hitting Bennu. The integral of the flux parametrization is in particles/($\text{m}^2 \text{ sr s}$) units, while N_p and N_α are in particles/s units. M is in MeV units as before.	52
5.1	Expected radionuclides in Bennu’s surface sample.	69

List of Figures

1.1	The OSIRIS-REx spacecraft in launch configuration (left) and sampling configuration (right). Image adapted from Bierhaus et al. (2018) [8].	6
1.2	(a) Typical NEA and PHO (b) Main Asteroid Belt and Trojan asteroids.	8
1.3	Image of Bennu collected by the OSIRIS-REx spacecraft from 24 km of distance. <i>Credits: NASA/Goddard/University of Arizona</i>	11
1.4	Projection of the candidate sampling sites' locations on the asteroid Bennu: Nightingale, Kingfisher, Osprey, and Sandpiper. <i>Credits: NASA/Goddard/University of Arizona</i>	13
1.5	Nightingale sampling site and sampling operations.	15
2.1	Floor plan of the Monte dei Cappuccini Laboratory. The tunnels of the air-raid shelter can be seen. The laboratory extends into the blue areas, with the entrance at the top left of the picture.	17
2.2	GEM 150	19
2.3	Study of the sample container.	20
3.1	CR flux-energy spectrum from G.A. Bazilevskaya and A.K. Svirzhevskaya (1998) [5].	24
3.2	Burger parametrization vs Castagnoli parametrization. The high-energies limit leads to the same values for both modulated and unmodulated LIS. As expected, high-energy particles are not influenced by the interplanetary magnetic field.	27

3.3	Leya's α parametrization vs Castagnoli's proton parametrization with a 660 MeV and a 330 MeV modulation parameters for protons and α -particles, respectively. In the next subsection, the fact that these two values correspond to the same solar activity intensity will be clear.	28
3.4	Castagnoli's parametrization for 5 modulation parameters values, from 200 to 1000 MeV.	30
3.5	BESS and PAMELA experimental results (points), which can be represented by the force-free approximation (continuous lines). The data from 1997 to 2009 allow for highlighting the GCR flux variation during a complete 11-year cycle. By following the chronological order of the data on the graph, it is easy to note the initial diminution of the flux intensity from 1997 to 2002 and then the ascent from 2004 to 2009. Figure adapted from Miyake, S., R. Kataoka, and T. Sato, (2017) [30].	31
3.6	Monthly mean sunspot number (blue) and modulation parameter (red) compared. It is clear from this image that a general correlation exists between the two series, both strictly linked to solar activity.	32
3.7	Covariance coefficient between yearly average sunspot number and reconstructed modulation parameter. We have a 0.7 coefficient with zero lag, which implies a high correlation between the two series. Moreover, we can see from non-zero lags that the strong oscillation reveals the presence of the dominant decadal cycle.	32
3.8	Saturation trend of the activity of a radionuclide with constant production rate. The x-axis is expressed in τ units, and the asymptote indicates the attainment of secular equilibrium, for which activity is equal to the rate of production.	35
3.9	Expected $^{22}\text{Na}/^{26}\text{Al}$ radioactivity ratio in Bennu in the past 150 years compared to the SN series. The same results for H and L chondrites can be seen in Taricco et al. (2010) [40].	38
4.1	^{26}Al and ^{22}Na SCR-induced radioactivities up to 5 cm of depth. . .	42
4.2	^{26}Al and ^{22}Na GCR-induced radioactivities up to 50 cm of depth. . .	43

4.4 Total radioactivity up to 50 cm of depth.	45
4.5 ^{26}Al radionuclides number depth distribution in Bennu. A total number of $5.8 \cdot 10^4$ nuclides were created in the asteroid by $4.4 \cdot 10^5$ incident protons, providing approximately one ^{26}Al isotope for every eight incident particles.	46
4.6 Isotropic irradiation from the source surface. Since the probability of emission is homogenous, the effect consists of denser field lines as the direction of emission approaches the tangent of the sphere. Image adapted from Santin (2007) [37].	47
4.7 Relationship between source surface and astroid radii and θ_{max} . Note that this logic is possible due to the fact that the asteroid and the source surface are concentric.	50
4.8 Geant4 hadronic models. Figure adapted from https://wuhongyi.cn/Geant4Note/PhysicsProcesses	53
4.9 Z-tests between the expected radioactivities from the Geant4 simulation and the measured radioactivities in the experiment. On the x-axis there are the mass numbers of the isotopes: ^{46}Sc , ^{48}V , ^{51}Cr , ^{52}Mn , ^{54}Mn , ^{56}Co , ^{57}Co , and ^{58}Co	55
4.10 Z-tests between the expected radioactivities from the Geant4 simulation and the measured radioactivities in the experiment. On the x-axis there are the mass numbers of the isotopes: ^{22}Na , ^{48}V , ^{51}Cr , ^{54}Mn	56
4.11 Test of the physics lists with the data from the Knyahinya chondrite. In this case, the <i>stairs plot</i> was used because the errors related to the counts in the histograms were neglectable.	57
5.1 Radioactivity in Bennu.	62
5.2 Comparison between the activities of ^{26}Al and ^{22}Na calculated with the Geant4 and Physical models.	64
5.3 Comparison between ^{26}Al and ^{22}Na α -induced and proton-induced activities in the Geant4 simulation. The ratio starts at a value of 0.16 for ^{26}Al and then seems to decrease to a constant asymptote. The same happens for ^{22}Na with lower values.	64

5.4	$^{22}\text{Na}/^{26}\text{Al}$ activity ratio for H, L, and CM chondrite compositions.	65
5.5	Reproduction of $^{22}\text{Na}/^{26}\text{Al}$ ratio.	67
5.6	^{26}Al and ^{22}Na mean activity as a function of depth.	69
5.7	Saturation trends for ^{26}Al and $^{22}\text{Na}/^{26}\text{Al}$. Note that the asymptote for the ratio is calculated with the expected total activity of the sample, which includes the SCR production and therefore is different from the ratio calculated for just the GCR production.	71
A.1	Classification of meteorites from Snelling (2015), adapted from Weisberg, McCoy, and Krot (2006) [48].	79

References

- [1] S. et al. Agostinelli. «Geant4—a simulation toolkit». In: *Nuclear Instruments and Methods in Physics Research Section A: Accelerators, Spectrometers, Detectors and Associated Equipment* 506.3 (2003), pp. 250–303. DOI: [10.1016/S0168-9002\(03\)01368-8](https://doi.org/10.1016/S0168-9002(03)01368-8) (cit. on p. 45).
- [2] J. et al. Allison. «Geant4 developments and applications». In: *IEEE Transactions on Nuclear Science* 53.1 (2006), pp. 270–278. DOI: [10.1109/TNS.2006.869826](https://doi.org/10.1109/TNS.2006.869826) (cit. on p. 45).
- [3] J. et al. Allison. «Recent developments in Geant4». In: *Nuclear Instruments and Methods in Physics Research Section A: Accelerators, Spectrometers, Detectors and Associated Equipment* 835 (2016), pp. 186–225. DOI: [10.1016/j.nima.2016.06.125](https://doi.org/10.1016/j.nima.2016.06.125) (cit. on p. 45).
- [4] E. Asvestari, I.G. Usoskin, G.A. Kovaltsov, M.J. Owens, N.A. Krivova, S. Rubinetti, and C. Taricco. «Assessment of different sunspot number series using the cosmogenic isotope ^{44}Ti in meteorites». In: *Monthly Notices of the Royal Astronomical Society* 467.2 (2017), pp. 1608–1613. DOI: [10.1093/mnras/stx190](https://doi.org/10.1093/mnras/stx190) (cit. on p. 33).
- [5] G.A. Bazilevskaya and A.K. Svirzhevskaya. «On The Stratospheric Measurements of Cosmic Rays». In: *Space Science Reviews* 85 (1998), pp. 431–521. DOI: [10.1023/A:1005029832052](https://doi.org/10.1023/A:1005029832052) (cit. on p. 24).
- [6] J. Beer, K. McCracken, and R. Steiger. *Cosmogenic radionuclides: theory and applications in the terrestrial and space environments*. Springer Science & Business Media, 2012 (cit. on p. 33).

- [7] N. Bhandari and M.B. Potdar. «Cosmogenic ^{21}Ne and ^2Ne depth profiles in chondrites». In: *Earth and Planetary Science Letters* 58.1 (1982), pp. 116–128. DOI: [10.1016/0012-821X\(82\)90107-8](https://doi.org/10.1016/0012-821X(82)90107-8) (cit. on p. 41).
- [8] E.B. Bierhaus, B.C. Clark, J.W. Harris, K.S. Payne, R.D. Dubisher, D.W. Wurts, R.A. Hund, R.M. Kuhns, T.M. Linn, J.L. Wood, A.J. May, J.P. Dworkin, E. Beshore, D.S. Lauretta, and the OSIRIS-REx Team. «The OSIRIS-REx Spacecraft and the Touch-and-Go Sample Acquisition Mechanism (TAGSAM)». In: *Space Science Reviewes* 214 (2018), p. 107. DOI: [10.1007/s11214-018-0521-6](https://doi.org/10.1007/s11214-018-0521-6) (cit. on pp. 5, 6).
- [9] G. Bonino, G.C. Castagnoli, and N. Bhandari. «Measurement of cosmogenic radionuclides in meteorites with a sensitive gamma-ray spectrometer». In: *Il Nuovo Cimento C* 15 (1992), pp. 99–104. DOI: [10.1007/BF02507775](https://doi.org/10.1007/BF02507775) (cit. on p. 17).
- [10] W.F. Bottke Jr., D. Vokrouhlicky, D.P. Rubincam, and D. Nesvorný. «THE YARKOVSKY AND YORP EFFECTS: Implications for Asteroid Dynamics». In: *Annual Review of Earth and Planetary Sciences* 34.1 (2006), pp. 157–191. DOI: [10.1146/annurev.earth.34.031405.125154](https://doi.org/10.1146/annurev.earth.34.031405.125154) (cit. on p. 5).
- [11] R. Burger, M. Potgieter, and B. Heber. «Rigidity dependence of cosmic ray proton latitudinal gradients measured by the Ulysses spacecraft: Implications for the diffusion tensor». In: *Journal of Geophysical Research* 105.A12 (2000), pp. 27447–27455. DOI: [10.1029/2000JA000153](https://doi.org/10.1029/2000JA000153) (cit. on p. 26).
- [12] K.N. Burke, D.N. DellaGiustina, K.J. Bennett C.A.;Walsh, M. Pajola, E.B. Bierhaus, M.C. Nolan, W.V. Boynton, J.I. Brodbeck, Jr. Connolly H.C., and et al. «Particle Size-Frequency Distributions of the OSIRIS-REx Candidate Sample Sites on Asteroid (101955) Bennu». In: *Remote Sensing* 13 (2021), p. 1315. DOI: [10.3390/rs13071315](https://doi.org/10.3390/rs13071315) (cit. on p. 12).
- [13] G. Castagnoli and D. Lal. «Solar Modulation Effects in Terrestrial Production of Carbon-14». In: *Radiocarbon* 22.2 (1980), pp. 133–158. DOI: [10.1017/S0033822200009413](https://doi.org/10.1017/S0033822200009413) (cit. on p. 26).

- [14] P. Colombetti, C. Taricco, N. Bhandari, A. Romero, N. Verma, and G. Vivaldo. «Experimental set-up for gamma-activity measurements of astromaterials». In: *2008 IEEE Nuclear Science Symposium Conference Record*. 2008, pp. 1802–1805. DOI: [10.1109/NSSMIC.2008.4774742](https://doi.org/10.1109/NSSMIC.2008.4774742) (cit. on p. 17).
- [15] P. Colombetti, C. Taricco, N. Bhandari, N. Sinha, M. Di Martino, A. Cora, and G. Vivaldo. «Low γ activity measurement of meteorites using HPGe–NaI detector system». In: *Nuclear Instruments and Methods in Physics Research Section A: Accelerators, Spectrometers, Detectors and Associated Equipment* 718 (2013), pp. 140–142. DOI: [10.1016/j.nima.2012.07.053](https://doi.org/10.1016/j.nima.2012.07.053) (cit. on p. 17).
- [16] G. Folger, VN Ivanchenko, and Johannes Wellisch. «The Binary Cascade: Nucleon nuclear reactions». In: *The European Physical Journal A - Hadrons and Nuclei* 21 (2004), pp. 407–417. DOI: [10.1140/epja/i2003-10219-7](https://doi.org/10.1140/epja/i2003-10219-7) (cit. on p. 53).
- [17] J. Gattacceca, F.M. McCubbin, J. Grossman, A. Bouvier, E. Bullock, H. Chennaoui Aoudjehane, V. Debaille, M. D’Orazio, M. Komatsu, B. Miao, and D.L. Schrader. «The Meteoritical Bulletin, No. 109». In: *Meteoritics & Planetary Science* 56.8 (2021), pp. 1626–1630. DOI: [10.1111/maps.13714](https://doi.org/10.1111/maps.13714) (cit. on p. 77).
- [18] Th. Graf, P. Signer, R. Wieler, U. Herpers, R. Sarafin, S. Vogt, Ch. Fleni, P. Pellas, G. Bonani, M. Suter, and W. Wölfli. «Cosmogenic nuclides and nuclear tracks in the chondrite Knyahinya». In: *Geochimica et Cosmochimica Acta* 54.9 (1990), pp. 2511–2520. DOI: [10.1016/0016-7037\(90\)90238-G](https://doi.org/10.1016/0016-7037(90)90238-G) (cit. on pp. 54, 56).
- [19] A Heikkinen, P Kaitaniemi, and A Boudard. «Implementation of INCL cascade and ABLA evaporation codes in Geant4». In: *Journal of Physics: Conference Series* 119 (2008), p. 032024. DOI: [10.1088/1742-6596/119/3/032024](https://doi.org/10.1088/1742-6596/119/3/032024) (cit. on p. 53).
- [20] F. Kondev, W. Meng, W. Huang, S. Naimi, and G. Audi. «The NUBASE2020 evaluation of nuclear physics properties». In: *Chinese Physics C* 45.3 (2021), p. 030001. DOI: [10.1088/1674-1137/abddae](https://doi.org/10.1088/1674-1137/abddae) (cit. on p. 36).

- [21] D. Lal and R.E. Lingenfelter. «History of the Sun during the Past 4.5 Gyr as Revealed by Studies of Energetic Solar Particles Recorded in Extraterrestrial and Terrestrial Samples». In: *The Sun in Time*. Ed. by C.P. Sonnett, M.S. Giampa, and M. S. Matthews. Tucson - AZ USA: University of Arizona Press, 1991, pp. 221–231. URL: https://books.google.it/books?id=GxW09WFoqV4C&pg=PA221&lpg=PA221&dq=History+of+the+Sun+during+the+Past+4.5+Gyr+as+Revealed+by+Studies+of+Energetic+Solar+Particles+Recorded+in+Extraterrestrial+and+Terrestrial+Samples&source=bl&ots=adNQhrrhg1&sig=ACfU3U010UUy085Lnllw3qo5tNKoXOMkxg&hl=it&sa=X&ved=2ahUKEwjF67-D3qb6AhV1Q_EDHX2FC6MQ6AF6BAgDEAM#v=onepage&q&f=false (cit. on p. 25).
- [22] D. S. Lauretta, C. D. Adam, A. J. Allen, R.-L. Ballouz, O. S. Barnouin, K. J. Becker, T. Becker, C. A. Bennett, E. B. Bierhaus, B. J. Bos, R. D. Burns, H. Campins, Y. Cho, P. R. Christensen, E. C. A. Church, B. E. Clark, H. C. Connolly, Jr., M. G. Daly, D. N. DellaGiustina, and K. . . . Yumoto. «Spacecraft sample collection and subsurface excavation of asteroid (101955) Bennu». In: *Science* 377.6603 (2022), pp. 285–291. DOI: [10.1126/science.abm1018](https://doi.org/10.1126/science.abm1018) (cit. on pp. 5, 6, 12, 69).
- [23] D. S. Lauretta, S. S. Balram-Knutson, E. Beshore, W. V. Boynton, C. Drouet d'Aubigny, D. N. DellaGiustina, H. L. Enos, D. R. Golish, C. W. Hergenrother, E. S. Howell, C. A. Bennett, E. T. Morton, M. C. search by orcid Nolan, B. Rizk, H. L. Roper, A. E. Bartels, B. J. Bos, J. P. Dworkin, D. E. Highsmith, D. A. Lorenz, L. F. Lim, R. Mink, M. C. Moreau, J. A. Nuth, D. C. Reuter, A. A. Simon, E. B. Bierhaus, B. H. Bryan, R. Ballouz, O. S. Barnouin, R. P. Binzel, W. F. Bottke, V. E. Hamilton, K. J. Walsh, S. R. Chesley, P. R. Christensen, B. E. Clark, H. C. Connolly, M. K. Crombie, M. G. Daly, J. P. Emery, T. J. McCoy, J. W. McMahon, D. J. Scheeres, S. Messenger, K. Nakamura-Messenger, K. Righter, and S. A. Sandford. «OSIRIS-REx: Sample Return from Asteroid (101955) Bennu». In: *Space Science Reviewes* 212 (2017), pp. 925–984. DOI: [10.1007/s11214-017-0405-1](https://doi.org/10.1007/s11214-017-0405-1) (cit. on pp. 5, 6).

- [24] D.S. Lauretta, Dani DellaGiustina, C. Bennett, D. Golish, K. Becker, S. Balram-Knutson, O. Barnouin, T. Becker, W. Bottke, William Boynton, H. Campins, Beth Clark, Connolly Jr, Christian Drouet d'Aubigny, Jason Dworkin, Joshua Emery, H. Enos, V. Hamilton, Carl Hergenrother, and Marc Bernacki. «The unexpected surface of asteroid (101955) Bennu». In: *Nature* 568 (2019), pp. 55–60. DOI: [10.1038/s41586-019-1033-6](https://doi.org/10.1038/s41586-019-1033-6) (cit. on p. 9).
- [25] I. Leya, J. Hirtz, and J.-C. David. «Galactic Cosmic Rays, Cosmic-Ray Variations, and Cosmogenic Nuclides in Meteorites». In: *The Astrophysical Journal* 910 (2021), p. 136. DOI: [10.3847/1538-4357/abe52f](https://doi.org/10.3847/1538-4357/abe52f) (cit. on pp. 26, 27, 29, 39, 45, 51, 54, 74).
- [26] K. Lodders. «Relative Atomic Solar System Abundances, Mass Fractions, and Atomic Masses of the Elements and Their Isotopes, Composition of the Solar Photosphere, and Compositions of the Major Chondritic Meteorite Groups». In: *Space Science Reviews* 217 (2021), p. 44. DOI: [10.1007/s11214-021-00825-8](https://doi.org/10.1007/s11214-021-00825-8) (cit. on p. 10).
- [27] R. Michel, P. Dragovitsch, P. Cloth, G. Dagge, and D. Filges. «On the production of cosmogenic nuclides in meteoroids by galactic protons». In: *Meteoritics* 26.3 (1991), pp. 221–242. DOI: [10.1111/j.1945-5100.1991.tb01043.x](https://doi.org/10.1111/j.1945-5100.1991.tb01043.x) (cit. on pp. 39, 41, 42).
- [28] R. Michel, I. Leya, and L. Borges. «Production of cosmogenic nuclides in meteoroids: accelerator experiments and model calculations to decipher the cosmic ray record in extraterrestrial matter». In: *Nuclear Instruments and Methods in Physics Research Section B: Beam Interactions with Materials and Atoms* 113.1 (1996), pp. 434–444. DOI: [10.1016/0168-583X\(95\)01345-8](https://doi.org/10.1016/0168-583X(95)01345-8) (cit. on p. 43).
- [29] R. Michel and S. Neumann. «Interpretation of cosmogenic nuclides in meteorites on the basis of accelerator experiments and physical model calculations». In: *Proc. Indian Acad. Sci. (Earth Planet Sci.)* 107.4 (1998), pp. 441–457. DOI: [10.1007/BF02841610](https://doi.org/10.1007/BF02841610) (cit. on pp. 25, 39, 42).
- [30] Shoko Miyake, Ryuho Kataoka, and Tatsuhiko Sato. «Cosmic ray modulation and radiation dose of aircrews during the solar cycle 24/25». In: *Space Weather* 15.4 (2017), pp. 589–605. DOI: [10.1002/2016SW001588](https://doi.org/10.1002/2016SW001588) (cit. on p. 31).

- [31] E.N. Parker. «The passage of energetic charged particles through interplanetary space». In: *Planetary and Space Science* 13.1 (1965), pp. 9–49. DOI: [10.1016/0032-0633\(65\)90131-5](https://doi.org/10.1016/0032-0633(65)90131-5) (cit. on p. 26).
- [32] P.N. Peplowski, J.T. Wilson, M. Burks, A.W. Beck, I. Jun, D.J. Lawrence, and Z.W. Yokley. «Cosmogenic radionuclide production modeling with Geant4: Experimental benchmarking and application to nuclear spectroscopy of asteroid (16) Psyche». In: *Nuclear Instruments and Methods in Physics Research Section B: Beam Interactions with Materials and Atoms* 446 (2019), pp. 43–57. DOI: [10.1016/j.nimb.2019.03.023](https://doi.org/10.1016/j.nimb.2019.03.023) (cit. on pp. 45, 46, 52, 54, 72).
- [33] S. Peracchi, J. Vohradsky, S. Guatelli, D. Bolst, L.T. Tran, D.A. Prokopovich, and A.B. Rosenfeld. «Modelling of the Silicon-On-Insulator microdosimeter response within the International Space Station for astronauts' radiation protection». In: *Radiation Measurements* 128 (2019), p. 106182. DOI: [10.1016/j.radmeas.2019.106182](https://doi.org/10.1016/j.radmeas.2019.106182) (cit. on pp. 47, 48).
- [34] J.M. Quesada, V. Ivanchenko, A. Ivanchenko, M.A. Cortés-Giraldo, G. Folger, A. Howard, and D. Wright. «Recent Developments in Pre-Equilibrium and De-Excitation Models in Geant4». In: *Progress in Nuclear Science and Technology* 2 (2011), pp. 936–941. DOI: [10.15669/pnst.2.936](https://doi.org/10.15669/pnst.2.936) (cit. on p. 53).
- [35] R.C. Reedy and J.R. Arnold. «Interaction of solar and galactic cosmic-ray particles with the Moon». In: *Journal of Geophysical Research (1896-1977)* 77.4 (1972), pp. 537–555. DOI: [10.1029/JA077i004p00537](https://doi.org/10.1029/JA077i004p00537) (cit. on pp. 37, 41, 66).
- [36] A.E. Rubin and J.N. Grossman. «Meteorite and meteoroid: New comprehensive definitions». In: *Meteoritics & Planetary Science* 45.1 (2010), pp. 114–122. DOI: [10.1111/j.1945-5100.2009.01009.x](https://doi.org/10.1111/j.1945-5100.2009.01009.x) (cit. on p. 6).
- [37] G Santin et al. «Normalisation modelling sources». In: *Geant4 tutorial, Paris* (2007) (cit. on p. 47).
- [38] K. Shibata, O. Iwamoto, T. Nakagawa, N. Iwamoto, A. Ichihara, S. Kunieda, S. Chiba, K. Furutaka, N. Otuka, T. Ohasawa, T. Murata, and H. Matsumoto. «JENDL-4.0: A New Library for Nuclear Science and Engineering». In: *Journal of Nuclear Science and Technology - J NUCL SCI TECHNOL* 48 (2011), pp. 1–30. DOI: [10.1080/18811248.2011.9711675](https://doi.org/10.1080/18811248.2011.9711675) (cit. on p. 54).

- [39] C. Taricco, N. Bhandari, D. Cane, P. Colombetti, and P. Verma. «Galactic cosmic ray flux decline and periodicities in the interplanetary space during the last 3 centuries revealed by ^{44}Ti in meteorites». In: *Journal of Geophysical Research* 45.A08102 (2006). DOI: [10.1029/2005JA011459](https://doi.org/10.1029/2005JA011459) (cit. on pp. 16, 17, 33).
- [40] C. Taricco, N. Bhandari, P. Colombetti, A. Romero, G. Vivaldo, N. Sinha, P. Jenniskens, M.H. Shaddad, and G.M. Ballabh. «Cosmogenic radioisotopes in the Almahata Sitta ureilite». In: *Meteoritics & Planetary Science* 45.10-11 (2010), pp. 1743–1750. DOI: <https://doi.org/10.1111/j.1945-5100.2010.01135.x> (cit. on pp. 16, 33, 38).
- [41] C. Taricco, N. Bhandari, P. Colombetti, N. Verma, and G. Vivaldo. «Experimental set-up and optimization of a gamma-ray spectrometer for measurement of cosmogenic radionuclides in meteorites». In: *Nuclear Instruments and Methods in Physics Research Section A: Accelerators, Spectrometers, Detectors and Associated Equipment* 572.1 (2007), pp. 241–243. DOI: [10.1016/j.nima.2006.10.359](https://doi.org/10.1016/j.nima.2006.10.359) (cit. on p. 17).
- [42] C. Taricco, P. Colombetti, N. Sinha, G. Vivaldo, and N. Bhandari. «a Large Cavity Gamma-Ray Spectrometer for Measurement of Cosmogenic Radionuclides in Astromaterials by Whole Rock Counting». In: Oct. 2007. DOI: [10.1142/9789812819093_0144](https://doi.org/10.1142/9789812819093_0144) (cit. on p. 17).
- [43] C. Taricco, N. Sinha, N. Bhandari, P. Colombetti, S. Mancuso, S. Rubinetti, and D. Barghini. «Early 18th century cosmic ray flux inferred from ^{44}Ti in Agen meteorite». In: *Astrophysics and Space Science* 361.338 (2016). DOI: [10.1007/s10509-016-2909-7](https://doi.org/10.1007/s10509-016-2909-7) (cit. on p. 33).
- [44] V. Ushinsky. «Development of the Fritiof model in Geant4». In: *Joint international conference on supercomputing in nuclear applications and Monte Carlo 2010 (SNA + MC2010)*. Hitotsubashi Memorial Hall, Tokyo, Japan, Oct. 2010. URL: <https://geant4.web.cern.ch/sites/default/files/geant4/results/papers/Fritiof-MC2010.pdf> (cit. on p. 54).
- [45] I. Usoskin, C. Taricco, N. Bhandari, and G. Kovaltsov. «Long-term solar activity reconstructions: Direct test by cosmogenic ^{44}Ti in meteorites». In:

- Astronomy & Astrophysics - ASTRON ASTROPHYS* 457 (2006), pp. L25–L28. DOI: [10.1051/0004-6361:20065803](https://doi.org/10.1051/0004-6361:20065803) (cit. on p. 33).
- [46] Ilya G. Usoskin, Galina A. Bazilevskaya, and Gennady A. Kovaltsov. «Solar modulation parameter for cosmic rays since 1936 reconstructed from ground-based neutron monitors and ionization chambers». In: *Journal of Geophysical Research: Space Physics* 116.A02104 (2011). DOI: [10.1029/2010JA016105](https://doi.org/10.1029/2010JA016105) (cit. on pp. 29, 30).
- [47] K.J. Walsh, R.-L. Ballouz, E.R. Jawin, C. Avdellidou, O.S. Barnouin, C.A. Bennett, E.B. Bierhaus, B.J. Bos, S. Cambioni, H.C. Connolly, M. Delbo, D.N. DellaGiustina, J. DeMartini, J.P. Emery, D.R. Golish, P.C. Haas, C.W. Hergenrother, H. Ma, P. Michel, and . . . D.S. Lauretta. «Near-zero cohesion and loose packing of Bennu’s near subsurface revealed by spacecraft contact». In: *Science Advances* 8.27 (2022), pp. 157–191. DOI: [10.1126/sciadv.abm6229](https://doi.org/10.1126/sciadv.abm6229) (cit. on pp. 5, 10).
- [48] Michael Weisberg, T. McCoy, and A. Krot. «Systematics and Evaluation of Meteorite Classification». In: *Meteorites and the Early Solar System II* 2 (2006), pp. 19–52. URL: <https://www.lpi.usra.edu/books/MESSII/9014.pdf> (cit. on p. 79).
- [49] D. Wright, T. Koi, G. Folger, V. Ivanchenko, M. Kossov, N. Starkov, A. Heikkinen, and H.-P. Wellisch. «Low and High Energy Modeling in Geant4». In: *AIP Conference Proceedings* 896 (2007). DOI: [10.1063/1.2720453](https://doi.org/10.1063/1.2720453) (cit. on p. 54).
- [50] D.H. Wright and M.H. Kelsey. «The Geant4 Bertini Cascade». In: *Nuclear Instruments and Methods in Physics Research Section A: Accelerators, Spectrometers, Detectors and Associated Equipment* 804 (2015), pp. 175–188. DOI: [10.1016/j.nima.2015.09.058](https://doi.org/10.1016/j.nima.2015.09.058) (cit. on p. 53).